# SPECTRAL MOMENTUM DENSITIES OF CRYSTALLINE GRAPHITE AND ION SPUTTERED AMORPHOUS CARBON FILMS FROM (e,2e) SPECTROSCOPY

by

Chao Gao

Dissertation submitted to the Faculty of the

Virginia Polytechnic Institute and State University

in partial fulfillment of the requirements for the degree of

Doctor of Philosophy

in

Physics

APPROVED:

A. L. Ritter, Chairman

R. Zaken

T. K. Lee

D. M. Hoffman

G. J. M. Indebetouw

August, 1988

Blacksburg, Virginia

**SPECTRAL MOMENTUM DENSITIES OF CRYSTALLINE GRAPHITE**

**AND ION SPUTTERED AMORPHOUS CARBON FILMS FROM (e,2e) SPECTROSCOPY**

by

Chao Gao

A. L. Ritter, Chairman

Physics

(ABSTRACT)

We have measured the spectral momentum density $\rho(E,\vec{q})$ of graphite by (e,2e) spectroscopy for momentum parallel and perpendicular to the crystal c-axis. In the independent electron approximation, $\rho(E,\vec{q}) = \sum_{\vec{K}} |U_{\vec{K}}(\vec{G})|^2 \times \delta(\vec{q} - \vec{K} - \vec{G})\, \delta(E - E(\vec{K}))$ where the one electron wave function is $\Psi_{\vec{K}}(\vec{r}) = e^{i\vec{K}\cdot\vec{r}} \sum_{\vec{G}} U_{\vec{K}}(\vec{G})\, e^{i\vec{G}\cdot\vec{r}}$ and $\vec{G}$ is a reciprocal lattice vector. The measurements covered a range of momentum parallel to the c-axis equal to $0 \leq |\vec{q}| \leq 1.84\text{Å}^{-1}$ and a range of momentum perpendicular to the c-axis equal to $0 \leq |\vec{q}| \leq 2.35\text{Å}^{-1}$. The energy range spanned the valence band of graphite from 4.4 eV above the Fermi energy to 27.6 eV below the Fermi energy. The momentum resolution was 0.47 $\text{Å}^{-1}$ and 0.73 $\text{Å}^{-1}$ (FWHM) for momentum parallel and perpendicular to the c-axis respectively. The energy resolution was 8.6 eV. The maximum coincidence rate was ~ 0.02 counts/second. The band structure $E(\vec{k})$ and spectral density $|U_{\vec{K}}(\vec{G})|^2$ have been calculated from first-principles using a self-consistent, density functional theory. The agreement within experimental uncertainties between measurement and theory is excellent.

We also have measured the spectral momentum density, $\rho(E,\vec{q})$, of ion sputtered amorphous carbon. Previous studies of this material have demonstrated that it is quite hard and nearly transparent while evaporated amorphous carbon is soft and dark. The local carbon - carbon bonding of ion sputtered a-C is thought to be a mixture of graphitic ($sp^2$) and diamond ($sp^3$) bonds. In the literature are claims that the concentration of $sp^3$ bonds can be as high as 75 % depending on the film making power. We find that in samples which optical measurements suggest have a high concentration of diamond bonding, our (e,2e)

measurements show nearly zero diamond bonding. The large difference between the properties of evaporated and ion sputtered carbon may be due to subtle differences between the electronic structure of the $\pi$ electrons in the two materials. We propose a new hybridization model of $\pi$ - $\sigma$ bond mixing for amorphous carbon which explains our data successfully.

# Acknowledgements

The author owes the deepest gratitude to his advisor, Dr. A. L. Ritter, for his valuable guidance and stimulating encouragement during completion of this work. Thanks are due to for Ramman measurements, for using EELS results prior to publication, and for help in TEM. Thanks also go to author's fellow graduate students for their assistance throughout the study.

Invaluable technical assistance provided by machine shop and electronics shop is greatly appreciated.

Financial support in part by the Grant No. DMR-8420555 from National Science Foundation is gratefully acknowledged. Graphite samples were prepared in part at national Nanofabrication Facility, which is supported by the National Science Foudation under Grant No. ECS-8619049.

Finally, the author would like to express a special thanks to his family for supporting in this study.

# Table of Contents

**I. Introduction** ..... 1

**II. Background** ..... 7

1. Theory of (e,2e) scattering ..... 7

2. Theory of graphite and diamond ..... 10

3. Models of amorphous carbon ..... 13

**III. Experiment** ..... 23

1. Experimental considerations ..... 23

2. Sample preparation and characterization ..... 25

3. Experimental results for graphite ..... 27

4. Experimental results for ion sputtered a-C ..... 28

**IV. Discussion and Conclusion** ..... 40

1. Discussion of graphite ..... 40

2. Discussion of ion sputtered a-C ..... 42

A. Band structure and sum rules ..... 42

B. Comparison with an angular average of graphite ..... 46
C. Hybridization model ..... 48
3. Conclusion ..... 51

**Bibliography** ..... 60

**Appendix A** ..... 68

**Appendix B** ..... 76

**Vita** ..... 87

# List of Illustrations

Figure 1. Block diagram of our (e,2e) Spectrometer. . . . . 6
Figure 2. Kinematics for (e,2e) and band structure of graphite . . . . . 19
Figure 3. Band structure of diamond . . . . . 20
Figure 4. Spectral momentum densities of graphite and diamond . . . . . 21
Figure 5. Raman spectra of our graphite sample and of a-C . . . . . 31
Figure 6. Experimental spectral momentum density of graphite . . . . . 32
Figure 7. Deconvoluted spectral momentum densities of graphite . . . . . 33
Figure 8. Experimental spectral momentum density of ion sputtered a-C . . . . . 34
Figure 9. Deconvoluted spectral momentum densities of ion sputtered a-C . . . . . 35
Figure 10. Spectral densities of graphite(parallel case) . . . . . 53
Figure 11. Spectral densities of graphite(perpendicular case) . . . . . 54
Figure 12. Experimental spectral densities of ion sputtered a-C . . . . . 55
Figure 13. The effective number of valence electrons . . . . . 56
Figure 14. The number of electrons occupying each band . . . . . 57
Figure 15. Experimental momentum densities of ion sputtered a-C . . . . . 58
Figure 16. Hybridized momentum densities of ion sputtered a-C . . . . . 59
Figure 17. Kinematics for multiple scattering . . . . . 86

# List of Tables

Table 1. Properties of different forms of carbon . . . . . 22

Table 2. Fitting parameters for graphite(parallel case) . . . . . 36

Table 3. Fitting parameters for graphite(perpendicular case) . . . . . 37

Table 4. Fitting parameters for high power ion sputtered a-C . . . . . 38

Table 5. Fitting parameters for low power ion sputtered a-C . . . . . 39

# I. Introduction

This dissertation presents the investigation of electronic structure of graphite and ion sputtered amorphous carbon by (e,2e) electron spectrometer. Our spectrometer has been described very detailed in refs.[1,2]. A block diagram of the Spectrometer is shown in Fig. 1. This is a new technique in condensed matter physics. Direct comparison between the theoretical spectral momentum density, $\rho(E, \vec{q})$, and the experimental coincidence count rate, $R(E, \vec{q})$, can be made as a function of binding energy $E$ and momentum $\vec{q}$ . The spectral density, $\rho(E, \vec{q})$, is the probability per unit energy and unit volume in momentum space of finding an electron with energy $E$ and momentum $\vec{q}$ in a system. In the independent electron approximation, $\rho(E, \vec{q})$ is the square of the one electron wave function in the momentum representation for states in the energy interval $E \rightarrow E + dE$.

The density of electronic states is given by

$$n(E) = \sum_{\vec{q}} \rho(E, \vec{q}) = \frac{2V}{(2\pi)^3} \int d\vec{q}\, \rho(E, \vec{q})$$

where $V$ is volume of the system. In a translationally periodic system, $\rho(E, \vec{q})$ is nonzero only along the line $E = E_n(\vec{q})$, where $\vec{q} = \hbar\vec{K} + \hbar\vec{G}_m$ and n is a band index($\vec{G}_m$ is a reciprocal

lattice vector and $\vec{K}$ is a wavevector in the first Brillouin Zone). It is the weight at a particular $E$ and $\vec{q}$ which reflects the component of the Block wave function of energy $E$ having real momentum $\vec{q}$.

In a disordered system, such as amorphous carbon, the wavevector is no longer a good quantum number and the spectral density, $\rho(E, \vec{q})$, spreads over regions of the $(E, \vec{q})$ space. At a particular energy there can be contributions from a finite range of momenta. The function $\rho(E, \vec{q})$ thus contains information about the momentum distributions, taking the place in disordered systems of the detailed Block wave function for the perfect lattice.

The spectral momentum density provides very detailed information about the electronic structure of solids. It can be calculated by Green's function methods[17] and can be measured only by (e,2e) spectroscopy. The band structure of crystalline solids can be measured by angle resoveled photo-electron spectroscopy(ARPES), but at this time information regarding the one electron wave functions can not be obtained from the intensity of the photo-emission peaks. The density of states can be measured by angle integrated photoemission. The integral of $\rho(E, \vec{q})$ over energy, the momentum density, can be obtained from Compton scattering and positron annihilation. The price one pays to measure the full spectral momentum density by (e,2e) spectroscopy is low count rate. The technique is a coincidence measurement, explained in more detail in the next chapter, and our maximum coincidence rate was approximately one event per minute. The experiment for graphite required four months of data taking. In order to obtain this rate, the energy resolution was $\Delta E = 8.6eV$ (FWHM) and the momentum resolution was estimated to be $0.47\text{Å}^{-1}$and $0.73\text{Å}^{-1}$ (FWHM) for momentum parallel and perpendicular to the crystal c-axis, respectively. The coincidence rate is proportional to $\Delta E \Delta q^4$. Possible ways to increase the data rate are being explored, but it is clear that in general most information regarding the electronic structure of crystalline solids can be obtained more expeditiously and with higher resolution by other techniques. Where (e,2e) spectroscopy provides fundamental insights is in the investigation of disordered solids. For example, in an initial experiment on amorphous carbon [16], two well defined bands were observed which did not broaden (within the

experimental resolution) even well out beyond the momentum of the crystalline Brillouin zone boundary. This counter intuitive result is being investigated theoretically [17,18].

The first (e,2e) measurements on solids were made over 15 years ago[19,20]. The energy resolution was not sufficient to resolve features in the valence band of the sample. In contrast, studies of gaseous atomic and molecular system have been very successful[29-31]. For example, excellent agreement between the (e,2e) cross-section and exact quantum calculations of hydrogen momentum wave functions has been found by Lohmann and Weigold[21]. The most complete (e,2e) study in solids to date was performed by Ritter et. al.[16] using evaporated amorphous carbon film ( $\sim$ 100Å). However, the validity of deriving (e,2e) cross-section in condensed matter remains unknown. It needs to be verified by a well characterized system, such as crystalline material. Using graphite as such system has three advantages. First, there is a mature theory of the electronic structure of graphite which agrees very well with existing experimental data. Secondly, it enables a comparison between results of the crystal form of carbon and the existing results of the amorphous form of carbon[16], which may lead to some significant conclusions regarding amorphous materials. And finally, it is easy to thin a layered material to a thickness of $\sim$ 100Å while retaining crystalline order.

We measured the spectral momentum density $\rho(E, \vec{q})$ of graphite by (e,2e) spectroscopy for one direction of momentum in the basal plane ($0 \leq |\vec{q}| \leq 2.35\text{Å}^{-1}$) and for momentum parallel to the c-axis ($0 \leq |\vec{q}| \leq 1.84\text{Å}^{-1}$). This is the first study of a crystal by this experimental technique. In the single particle approximation the spectral density is equal to $|\Phi_{\vec{K}}(\vec{q} = \vec{k} + G_{\vec{m}})|^2$ when $E = E_n(\vec{k})$ . The spectral density of graphite has been calculated from first-principles using self-consistent, density-functional theory in the local-density approximation with a mixed-basis pseudopotential technique. Excellent agreement is found within the experimental uncertainties between theory and the measurements reported here. The same theoretical approach has been used to calculate the band structure and charge density of graphite [3]. The band structure has been measured by several groups using angle resolved photo-electron spectroscopy (ARPES) for electron

momentum in the basal plane of the crystal[4-13]. The difference between theory and these measurements is less than or of order 1 eV. There is also good agreement between the calculated and measured charge density[3]. The density functional technique has been used to calculate the ground state properties of many solids and the agreement with measurements is often within a few percent. Thus, from our perspective, a mature theory of graphite exists and has been confirmed well by several independent experiments. We view the calculated spectral density as a benchmark for evaluating this new experimental technique, (e,2e) spectroscopy. The agreement between our measurements and theory is strong evidence that the analysis [14,15] relating the (e,2e) coincidence rate to the spectral momentum density is correct.

We also measured the spectral momentum density, $\rho(E, \vec{q})$, of two forms of ion sputtered amorphous carbon films for momentum $0. \leq |\vec{q}| \leq 3.75\text{Å}^{-1}$. One was made at low RF power (200 W), referred to as the low power sample. The other was made at high RF power (1000 W), referred to as the high power sample. The first conditions generally produce hard films with high resistivity while the second conditions produce softer films with low resistivity[22,23]. Our (e,2e) results are very similar to the spectral density of graphite except at small q around 8 eV. The spectral momentum densities in this region of phase space are significantly larger than those of graphite. Previous studies of these materials have demonstrated that they are quite hard and nearly transparent while evaporated a-C is soft and dark. The local carbon - carbon bonding of ion sputtered a-C is thought to be a mixture of graphitic ( $sp^2$ ) and diamond ( $sp^3$ ) bonds; and according to indirect experimental measurements, the concentration of $sp^3$ bonds can be as high as 75 % depending on the film making power. We find that the bonding is almost entirely graphitic in our samples, which is contrary to the optical result of Savvides [22,23] and the EELS result of Fink et al.[70,71]. The study by Fink et al. was done on hydrogenated amorphous carbon and may not be directly applicable to our results. The large difference between the properties of evaporated and ion sputtered carbon may be due to subtle differences between the electronic structures

of the $\pi$ electrons in the two materials. Based on the strained layer model of Egrun[80,85] and on the suggestion of Haydock[18], we compare the observed spectral momentum density with an angular average of the graphite bands and propose a new hybridization model of $\pi$ mixing with $\sigma$ bonds for amorphous carbon which explains our data successfully.

The rest of this dissertation is organized as follows. The second chapter deals with the theory of (e,2e) scattering from solids, describes the details of calculating the spectral momentum densities of graphite and diamond, and discusses various models for the electronic structure of amorphous carbon. Details of sample preparation and the experimental results are given in the third chapter. The experimental data are analyzed and the results summarized in the fourth chapter. The effects of multiple scattering and multiple dimensional integrals are presented in appendix a and appendix b, respectively.

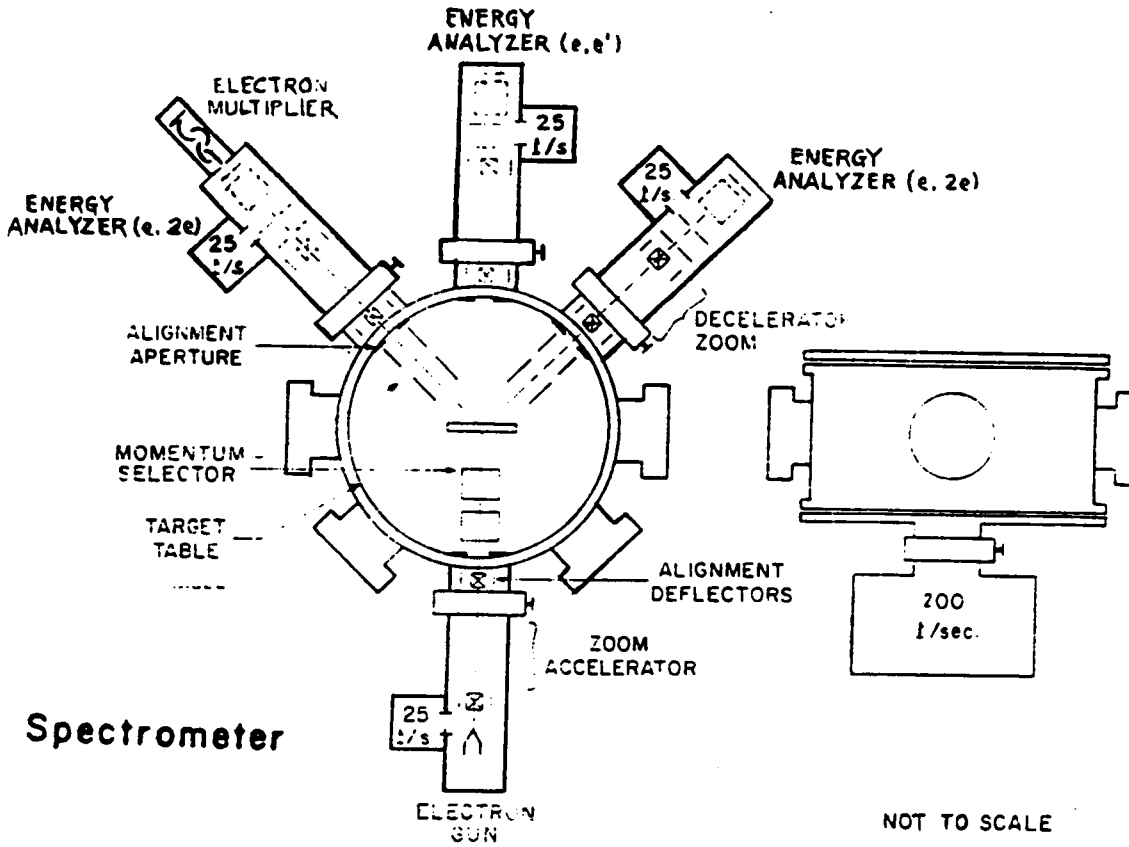


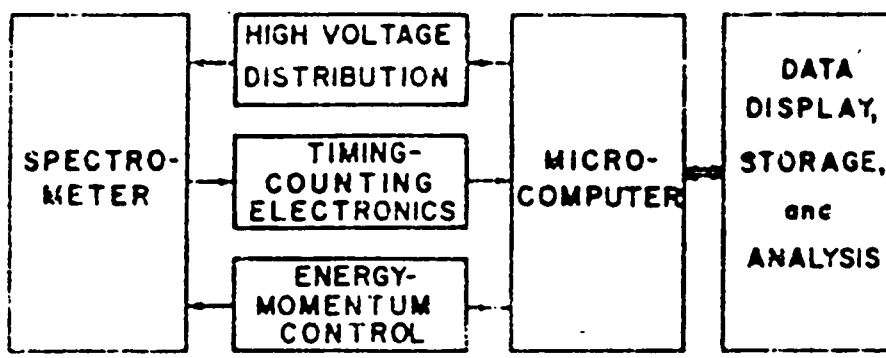


Fig. 1. Block diagram of our (e,2e) Spectrometer[1,2].

# II. Background

## *1. Theory of (e,2e) scattering*

In (e,2e) analysis there are three dominant electron scattering processes which can be identified as elastic, inelastic, and (e,2e) scattering. Elastic scattering is mainly coherent Bragg scattering at small angles and becomes incoherent Rutherford scattering from target nuclei at large angles. In small-angle inelastic scattering, a small momentum coupled with an energy loss is transferred to the target. Detailed calculation of the total small-angle inelastic scattering is given in refs.[24-26,103]. Plasma excitation and interband transitions have the largest cross section in forward scattering. The large-angle inelastic scattering process involves the incident electron knocking off a target electron. In the plane-wave impulse approximations the scattering probability is given by the Mott cross-section. An (e,2e) scattering event can be defined as a large-angle inelastic scattering event in which the kinematics of incident, scattered, and recoiling electrons are fully determined by conservation of energy and momentum (see Fig. 2).

In a typical (e,2e) experiment on a thin film, the target thickness is much less than the mean free path of large-angle scattering and is comparable to the mean free path of small-

angle scattering. Therefore, in an (e,2e) experiment it is only small-angle collisions which contribute significantly to the multiple scattering background. An electron which scatters by a large angle may have one or more small-angle collisions before or after the large angle vertex. Similarly, the recoiling electron may suffer one or more collisions before leaving the film. A general procedure for correcting multiple scattering has been given by Jones and Ritter[101].

The kinematics for (e,2e) scattering are shown in Fig. 2(a). The energy of the incident electron is 25 KeV. The angles of the scattered and recoiling electrons are $\theta_1 = \theta_2 \simeq 45°$ so that the energies of the outgoing electrons are ~12.5 KeV. The precollision binding energy and momentum of the ejected electron is determined by conservation of energy and momentum. Electrons in the target with momentum perpendicular to the incident beam direction can be observed by varying the angle $\delta$. Electrons with momentum parallel to the incident beam can be detected by varying $\theta_1$ and $\theta_2$ symmetrically about 45°. The cross section for (e,2e) scattering from a target electron with binding energy $\varepsilon$ and real momentum $\vec{q}$ is [15]

$$\frac{d\sigma}{dE_1 dE_2 d\Omega_1 d\Omega_2} = \frac{m|\vec{P}_1||\vec{P}_2|}{\hbar^3|\vec{P}_0|}\left[\frac{d\sigma}{d\Omega}\right]_M \left|F(\vec{q}=\vec{P}_1+\vec{P}_2-\vec{P}_0)\right|^2$$

$$\times \delta(E_1 + E_2 - E_0 - \varepsilon) \qquad [II.1]$$

with

$$\left[\frac{d\sigma}{d\Omega}\right]_M = \left[\frac{e^2}{4E_0}\right]^2 \times 4\cos\theta\,[\,\sin^{-4}\theta - (\sin\theta\,\cos\theta)^{-2} + \cos^{-4}\theta] \qquad [II.2]$$

where $[d\sigma/d\Omega]_M$ is the Mott electron-electron cross section which is a function of the scattering angle $\theta$ between $\vec{P}_0$ and $\vec{P}_1$ in the Lab frame. The function $|F(\vec{q})|^2$ is the momentum density of the one electron target orbital $\Psi_\alpha(\vec{r})$

$$F(\vec{q}) = (1/2\pi)^{3/2} \int e^{-i\vec{q}\cdot\vec{r}}\ \Psi_{\alpha}(\vec{r})\, d\vec{r} \qquad [II.3]$$

where in a crystal, the one electron orbital can be written as a Bloch wave function

$$\Psi_{\vec{k},n} = e^{i\vec{k}\cdot\vec{r}}\ U_{\vec{k},n}(\vec{r}) = \sum_{\vec{G}} U_{\vec{k},n}(\vec{G})\ e^{i(\vec{k}+\vec{G})\cdot\vec{r}} \qquad [II.4]$$

so that

$$|F(\vec{q})|^2 = \sum_{\vec{G}} |U_{\vec{k},n}(\vec{G})|^2 \delta(\vec{q} - \vec{k} - \vec{G}) \qquad [II.5]$$

Thus, the spectral momentum density is a map of the band structure in the repeated zone representation with the intensity equal to the square of the fourier expansion coefficient. In deriving the cross section, two approximations were made that require experimental verification. The first approximation is that the incident, scattered and recoiling electron can be represented by plane waves. There have been several studies of atomic and molecular systems [29-31] which indicate that the plane-wave approximation is good when the incident electron energy is greater than ~ 2 KeV. The energy of the incident electron is an order of magnitude larger than this lower limit in our case so that the plane wave approximation should be quite accurate. The second assumption, the impulse approximation, is that at large scattering angles and for incident energies much larger than the binding energy of the recoiling electron, the spectator electrons are frozen while the collision takes place. In other words, the single particle states of all electrons except the incident and recoiling electrons do not change during the collision. This typically is not a good approximation in strongly correlated systems such as atoms, molecules, and narrow d and f bands of solids. In these cases "satellite" peaks to the single particle spectrum are ob-

served which arise from the excitation of spectator electrons during the collision process. These shake-up processes rarely occur in weakly correlated S and P valence bands of solids. Consistent with this general observation, we do not observe any structure in our (e,2e) data which could be associated with multi-electron excitations. The good agreement between our measurements and the spectral momentum density predicted on the basis of the single-particle approximation is strong evidence that the approximations in the derivation of the (e,2e) cross section are valid.

Finally, in our scattering geometry the proportionality constant between the spectral momentum density and the (e,2e) coincidence rate is nearly independent of the target electron momentum $\vec{q}$ which is being observed. The proportionality constant does depend on q because of the angular dependence of the Mott cross section, but the dependence is very weak. The Mott cross section changes by less than 6% as we sweep from $q = -3$ Å$^{-1}$ to 3 Å$^{-1}$. Thus, to an excellent approximation the measured coincidence rate is a direct map of the spectral momentum density. It is difficult to make an absolute determination of the proportionality constant between coincidence rate and spectral momentum density, but it is the relative variation of $|F|^2$ with energy and momentum which is of primary interest and this quantity can be measured accurately.

# 2. Theory of graphite and diamond

Carbon in its crystalline form can exist either in three-fold coordination as graphite, a semimetal, or in four-fold coordination as diamond, a wide bandgap semiconductor. Group IV elements with four valence electrons are expected to form four bonds. As $\sigma$ bonds are more stable than $\pi$ bond, one might think the diamond lattice with its four $\sigma$ bonds per site to be the most stable. Recently, realistic total-energy calculations for group IV elements in a variety of crystalline lattice have been carried out by Yin and Cohen[27]. Si and Ge are found

to be more stable in the diamond lattice and less stable in the three-fold coordinated graphite structure or the six-fold simple cubic lattice. Carbon is atypical in that it is slightly more stable in the graphite lattice, and increasingly unstable in a lattice of high coordination. The fundamental reason for this behavior is that only the first row elements are missing *P* -like core electrons[28]. This causes their valence *P* orbital to be more compact and more tightly bound, compared to the *S* states. This effect strengthens carbon's $sp^2$ bonds compared to its $sp^3$ bonds, and favors the graphite structure.

Graphite as a prototype of the layered structure has attracted considerable attention both theoretically and experimentally during the last decades. It has not only potentially important technological applications but also provides a realistic situation for the fundamental study of two dimensional phenomena. It has a crystal structure built up of flat layers in which the trivalent carbon atoms occupy the lattice sites of a two dimensional honeycomb network. The layers are stacked in a hexagonal crystal structure corresponding to the space group $P6_3/mmc$ ( $D_{6h}$ ). Half the carbon atoms are located directly above each other in the adjacent planes and half are located above the centers of the hexagonal cells in the adjacent planes. The unit cell has four atoms: two from each contributing layers, and each atom contributes four electrons to form valence bands in graphite. In single crystals of graphite, the shortest interatomic distance is 1.42Å in the planes, while the distance between the consecutive planes is 3.354Å . Bonding within the layers is strong and is described by $sp^2$ hybridized $2s$, $2p_x$ and $2p_y$ atomic orbitals. The bonding between layers is weak, originating from the overlap between $2p_z$ orbitals. The resulting band structure consists of manifold six $\sigma$ bands and two $\pi$ bands forming the filled valence band, above which lies the conduction band consisting of the corresponding anti-bonding $\sigma$ and $\pi$ bands.

The band structure of graphite has been calculated by several groups [3,32-39]. Holzwarth, et al. used a first-principles, self-consistent technique which has been very successful in describing many ground state properties of crystalline solids. The technique is based on density-functional theory in the local- density approximation (Hedin-Lundques approximation) using the mixed-basis pseudopotential approach. In addition to the band

dispersion relations, the expansion coefficients for the band wave functions come out directly from these calculations. In Figs. 2(b) and (c) are shown the Brillouin zone of graphite and the band structure for particular symmetry directions. The six $\sigma$ valence bands, based on $sp^2$ orbitals in the basal plane, are shown as solid lines, while the two $\pi$ valence bands from the $P_z$ atomic orbitals are represented by dashed lines. Due to the weak interlayer interaction, the electronic structure is nearly two dimensional collapsing the number of valence bands to three $\sigma$ bands and one $\pi$ band. The spectral densities of graphite bands are shown as solid lines in Fig. 4. The spectral densities of the $\sigma$ and $\pi$ bands are shown in Fig. 4(a) for momentum in the basal plane ($\Gamma \rightarrow M$). The wave functions for the lowest $\sigma$ bands are S-like, that is the momentum density is maximum at q = 0 and decreases monotonically as q increases. The wave functions for the upper two $\sigma$ bands are P-like. The momentum density of the $\sigma_2$ band is zero at q = 0, rises abruptly near the Brillouin zone boundary to a peak in the second zone, and then falls off exponentially as $q \rightarrow \infty$. The momentum density of the $\sigma_3$ band peaks in the third zone. The spectral densities in the $\Gamma \rightarrow K$ direction are shown in Fig. 4(b). They are qualitatively similar to the momentum densities in the $\Gamma \rightarrow M$ direction. The momentum density of the $\pi$-band is zero for $\vec{q}$ in the $\Gamma - K - M$ plane because the $\pi$ -orbital has a node there. In Fig. 4(c) are the spectral momentum densities for $\vec{q}$ along the c-axis in the $\Gamma - A$ direction. The bands are quite flat in this direction dispersing less than or of order 1 eV. The momentum density of the lowest $\sigma$ band again falls off monotonically from q = 0. The momentum densities of the upper $\sigma$ bands are zero for $\vec{q}$ along the c-axis for symmetry reasons. The momentum density of the $\pi$ -band displays P-wave character; it is zero at the origin and peaks in the third zone at $q \simeq 1.5 \text{Å}^{-1}$. From these calculations one can see that graphite is an interesting blend of nearly free-electron behavior for $\vec{q}$ in the crystal plane and atomic character for momentum perpendicular to the crystal plane.

Diamond has a fcc crystal structure and there are two atoms per unit cell. The atoms are in tedrahedral bonding with a nearest neighbor distance of 1.54 Å. Using the same technique as for graphite,

Holzwarth[42] has calculated the band structure and the spectral momentum densities for diamond. In Figs. 3(a) and (b) are shown the Brillouin zone of diamond and the band structure for particular symmetry directions. The valence electrons form four $\sigma$ bands, based on $sp^3$ orbitals. The spectral densities of diamond bands are shown as dashed lines in Fig. 4. The spectral densities of bands are shown in Fig. 4(a) for the $\Gamma \rightarrow L$ direction. The wave functions for the lowest $\sigma$ bands are S-like, that is the momentum density is maximum at q = 0 and decreases monotonically as q increases. The wave functions for the upper three $\sigma$ bands are P-like. The momentum density of the $\sigma_2$ band is zero at q = 0, rises abruptly near the Brillouin zone boundary to a peak in the second zone, and then falls off exponentially as $q \rightarrow \infty$. The momentum density of the $\sigma_3$ band peaks in the third zone and the $\sigma_4$ band peaks in the fourth zone. The spectral densities in the $\Gamma \rightarrow K$ and $\Gamma \rightarrow X$ direction are shown in Figs. 4(b) and (c), respectively . They are qualitatively similar to the momentum densities in the $\Gamma \rightarrow L$ direction. From Fig. 4 the spectral momentum densities of $\sigma$ bands in graphite and diamond are very similar to each other within our resolution. In diamond there is nothing in the region of the $\pi$ band in graphite for $q \leq 1.5 \text{Å}^{-1}$. From our experimental point of view this is the major difference between graphite and diamond that we can observe in our measurements. The difference between the valence band width of graphite and diamond is on the borderline of our statistical accuracy.

# 3. Models of amorphous carbon

Carbon exists not only in the crystalline form but also in the amorphous state and may possess intermediate properties between graphite and diamond. The properties of a-C depend on the preparation methods. Different kinds of a-C have been classified as glass carbon, evaporated a-C, ion sputtered carbon, and hydrogenated a-C. Glass carbon can be formed by heating certain organic polymers[43]. Evaporated a-C can be obtained by using

evaporation and arc discharge[44] and by using high ion energy ( ~ 3000 eV ) sputtering from a carbon cathode[45]. Those two kinds of a-C are polymer-like(i.e., electrically insulating, soft, and optically trasparent) or graphitic (i.e., electrically conductive, soft, and optically opaque). Two other types of carbon film which were produced by using low ion energy sputtering or by cracking hydrocarbon gases with a negative bias in dc or rf plasma modes[46-49] are described as ion sputtered a-C and hydrogenated a-C, respectively. Those two kinds of a-C are diamondlike (i.e. electrically insulating, hard, and optically transparent). Table 1 shows some physical properties of different forms of carbon. The two carbon films we studied were made by a low energy ion beam technique and fall in the diamondlike carbon category because their properties are closer to those of diamond than those of graphite.

The first reports on the formation of dense, inert and glassy carbon films date back more than three decades[50]. Schmellenmerier[51,52] was the first person to apply deposition from a d.c. plasma sustained in $C_2H_2$ to prepare carbon films in which he conjectured the presence of diamond-like constituents. The topic has received steadily increasing attention since Aisenberg and Chabot[46,47] in the early seventies published their findings on the formation of diamond-like carbon films by the condensation of energetic carbon ions onto various substrates. Within the last decade many investigations have confirmed that very hard and electrically insulating carbon layers are obtained when ionized hydrocarbon species[53-58] or carbon ions of sufficient energy are deposited[59-62]. Moreover, Weissmantel et al. demonstrated that ion beam sputter deposition of carbon under simultaneous bombardment by energetic inert gas ions ( $Ar^+, Kr^+$ ) yields films of a similar type[63] . Recently, it has been reported that polycrystalline films of true diamond structure have been prepared by vapor-deposition[65].

The diamondlike properties of a-C raise a very interesting question about the bonding of carbon atoms because the atoms in graphite are all in $sp^2$ bonding and the atoms in diamond are all in $sp^3$ bonding. Robertson[64] has discussed the possible bonding of a carbon atom. In principle, a carbon atom can have three bonding configurations, $sp^1$, $sp^2$ and $sp^3$. At a carbon $sp^1$ site, two of the four valence electrons form $\sigma$ bands along $\pm p_x$, and the other

two electrons are left in orthogonal $p_y$ and $p_z$ orbitals to form $\pi$ bands. At $sp^2$ sites three electrons are assigned to the trigonally directed $sp^2$ hybrids which form $\sigma$ bands; the fourth electron lies in a $p_z$ orbital lying normal to the $\sigma$ bonding plane. The $p_z$ orbital forms weaker $\pi$ bonds with adjacent $p_z$ orbitals. In the $sp^3$ site, all of the four electrons are assigned to tetrahedrally directed $sp^3$ hybrid orbitals which then form strong $\sigma$ bonds with adjacent atoms. It is generally believed that atoms in evaporated a-C are mainly in $sp^2$ bonding since the properties of this kind of a-C are very similar to those of graphite. Zelez and Savvides[66,22] demonstrate that ion-assisted deposition greatly changes the properties of a-C close to those of diamond. This leads them to hypothesize that the fraction of $sp^3$ sites in a-C increase under ion-assisted deposition. They suggest the following mechanism for producing the $sp^3$ bonds. In evaporation the incident particles only have thermal energies. However, in plasma deposition the major species in the plasma are believed to be radicals[67,68]. A physical deposition regime now exists with radicals arriving directly from the bulk plasma at the substrate. The bias voltage also gives the positive ions incident on the substrate with a higher kinetic energy. According to the model of Weissmantel[63], the incident particles cause an intense local thermal and pressure spike. Noting that diamond is stable in the high temperature high pressure zone of carbon's phase diagram, Weissmantel asserts that the spike favors the formation of $sp^3$ sites. This results in a higher fraction of $sp^3$ sites which make film 'diamondlike'.

A great number of analytical techniques have been employed recently to characterize film microstructure including a) Raman , ESR, and EELS measurements[62,69-74], b) transmission electron diffraction and x-ray photoemmision spectroscopy [75,76], and c) optical specotrscopy[62,73,77,78]. What has emerged from these studies is that different film deposition techniques and system configurations lead to highly variable film properties. It is believed that various forms of amorphous carbon have similar short range structure(either tetrahedral or graphitic bonds) with differences which depend on the starting material, on the method of preparation and on the heat treatment temperature[43,78,79]. There thus remains

some uncertainty concerning bonding and the origin of diamond-like properties in a-C films. This uncertainty suggests that research on solid carbon is far from being terminated.

Based on X-ray, electron and neutron diffraction[80-85], several models have been proposed for the microstructure of a-C. In the strained layer model of Egrun[80,85], the glassy carbon consists of strained graphite layers stacked in a disordered manner. There is no $sp^3$ in this model. Using this model, Egrun reproduced the experimental diffraction intensity F(k) of his glassy carbon sample. Stenhouse and Grout[86] tried to develop a theory which would handle a greater degree of disorder. They postulated that a-C could be modelled by considering it as a microcrystalline of graphite inter-linked by an $sp^3$ banded random network. They calculated the radial distribution function(r.d.f.) as a function of microcrystallite size and the proportion of $sp^3$ sites. Then, diffraction intensities can be obtained from the r.d.f.. Stenhouse and Grout compared calculated intensities with those measured by Kakinoki et al.[82] and Franklin[87]. They concluded that the Kakinoki sample contained about 75% $sp^3$ sites and had 12 Å graphitic domains, while the Franklin sample had about 50 % $sp^3$ and 20Å domains. However, Mildner and Carpenter[84] and Summerfild et al. [88] found an error in the analysis of Stenhouse and Grout which caused them to over estimate the importance of $sp^3$ regions in the case of small crystallines. Beeman et al.[89] considered even more disordered structures. They constructed four model random networks containing different proportions of $sp^2$ and $sp^3$ sites. The model which contains only $sp^3$ is just the Polk [90] model rescaled from Ge to carbon. After an extensive comparison with r.d.f., Robertson[64] concluded that the random network models of Beeman et al. are valuable in pointing out the types of disorder present in evaporated a-C, but they probably possess insufficient correlations between their $sp^2$ sites.

The existence of a distinct graphitic phase interspersed in a diamondlike medium and vice versa also has been proposed[79,82,86,89,91] for ion sputtered a-C, but convincing experimental proof is lacking. The boundary between two regions would consist of defective bonds. Its bonding microstructure has been of intense interest and speculation for more

than a decade [79,82,86]. Recently, based on EELS and optical data, Fink et. al[70,71] and Savvides[22,23] estimated the proportion of $sp^3$ bonding in a-C by using sum rules.

The existence of bands structure in amorphous solids has been discussed by Ziman[92,93], Beeby et al.[17] and Haydock[18]. Ziman argues that the coherence length for the phase of one electron wave function is finite. This corresponds to a broadening in momentum space of the crystalline delta function wavepacket. It is understandable, because the wavenumber is no longer a good quantum number in disordered system. Moreover, it is argued that at small q, that is for wavelength much longer than the dimension of potential fluctuations, electrons in amorphous materials propagate in an effective medium which is not significantly different from the crystal lattice. This implies that the spectral momentum densities of a-C near $q = 0$ should be those of graphite or diamond. Our results show that this is not the case because the spectral momentum densities of both graphite and diamond are much smaller than those of a-C near $q = 0$ and around $E_B = 8eV$. It also implies that graphite and diamond should have the same band structure at $q = 0$ which is obviously not right. Ziman also argues that when q gets larger, that is the wavelength getting shorter, electrons suffer more scattering by disorders in propagation. Therefore, the coherence length is getting shorter. This means that the wavepacket of electrons is getting broader in momentum space. When the coherent length approaches the correlation length of potential fluctuations, the bands in an amorphous material will coalesce. In the disordered system, the spectral momentum density should be $\rho(E, \vec{K})$ instead of $\rho(\vec{K})\delta[E - E(\vec{K})]$ for a perfect lattice. That is, $\rho(E, \vec{K})$ for the crystalline phase is nonzero only along the dispersion curve $E(\vec{K})$ . In the disordered system, $\rho(E, \vec{K})$ spreads over regions of $(E, \vec{K})$ space. At a particular energy there can be contributions from a finite range of momenta. Beeby et al.[17] have calculated this distribution function by Greens function methods for the tetrahedrally bonded amorphous. Their results show that there is indeed a well defined band corresponding to the lowest energy crystal valence band which generally has S-wave symmetry. The less spherical P-like bands at the top of the valence band are more diffuse. Recently, Haydock[18] proposed a theory for amorphous systems and applied it to a particular model. His model is a 2-D graphite

structure in which two hexagonal rings have been replaced by a 5-fold and a 7-fold rings. The translational symmetry is broken, but Haydock finds another operator, $S$ , which commutes with the Hamiltonian and is analogous to the translation operator. The operator $S$ can be written as $S = \sum_s t_s$ ; here each $t_s$ maps orbitals from one site to another. But, here the sum may include several mappings from and to each site, and even several different mappings between the same pair of sites. He assumes that each atom has a similar local environment throughout the structure, and concludes that the eigenfuctions of $S$ and H in the momentum representation consist of concentric fuzzy spheres of finite thickness, possibly overlapping. He defines the magnitude at the first maximum as 'network momemtum' which is analogous to the definition of the crystal momentum as the momentum of the site nearest zero in reciprocal lattice of momenta contributing to a Bloch state. The dispersion relation between energy and "network momentum " is very similar to an angular average of the graphite band structure and agrees very well with the (e,2e) experiment on evaporated a-C[16].

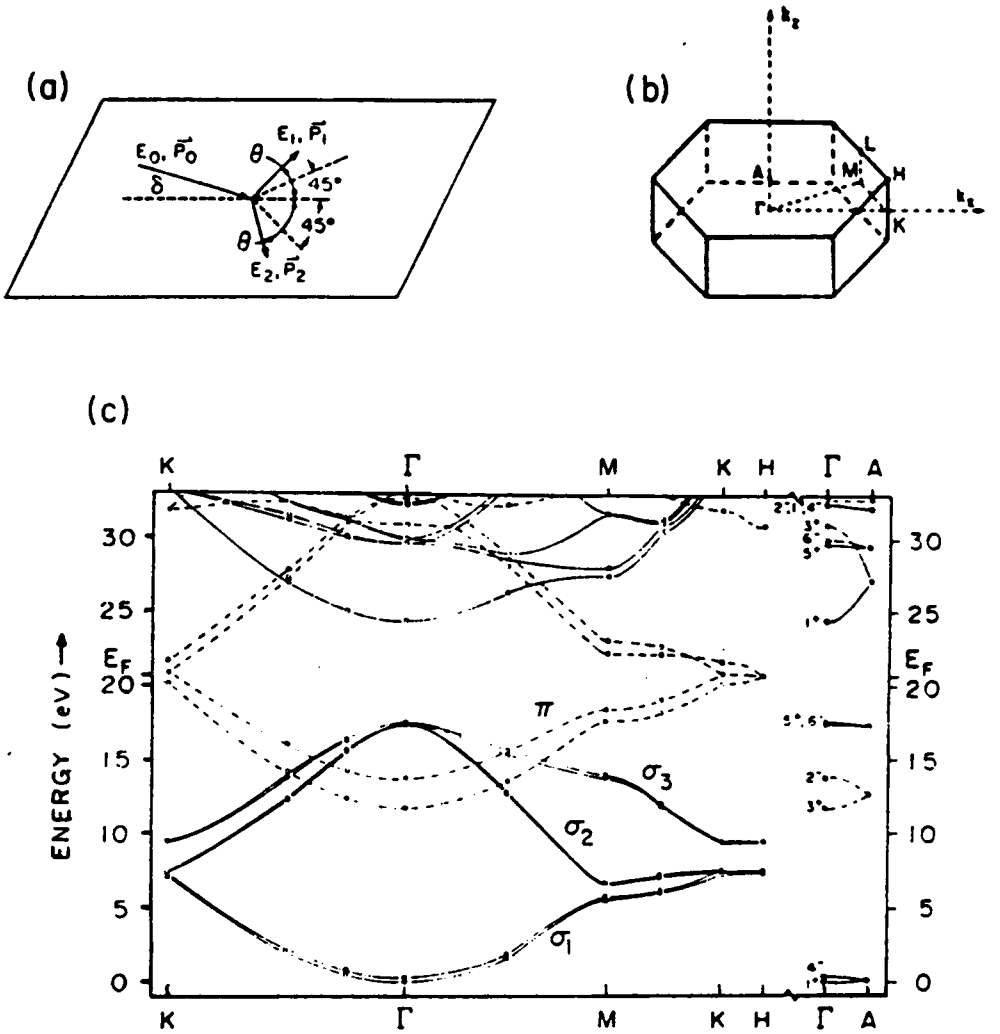


Fig. 2. (a) Kinematics for (e,2e) scattering. (b) Brillouin zone of graphite. (c) Band structure of graphite.

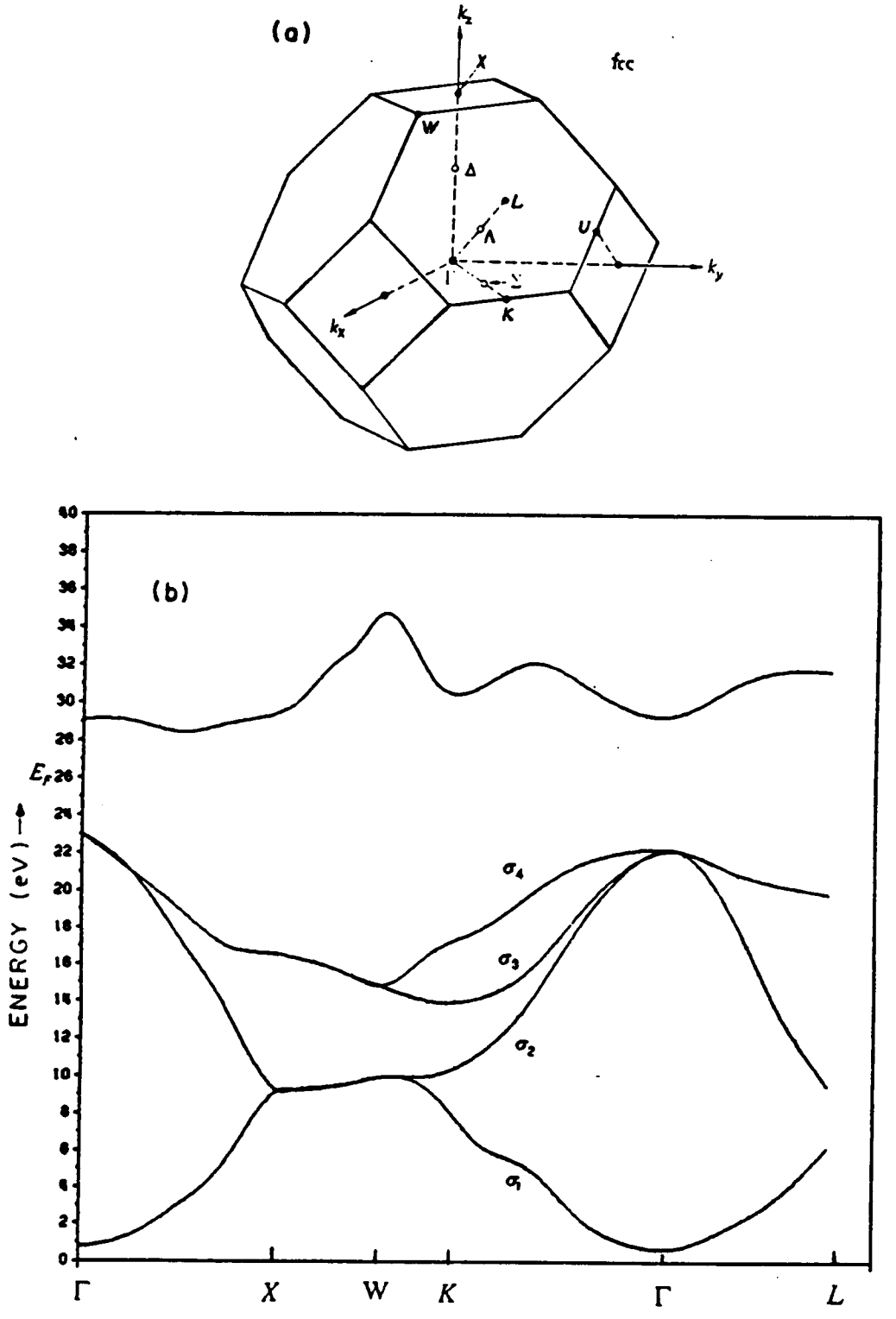


Fig. 3. (a) Brillouin zone of diamond. (b) Band structure of diamond[42].

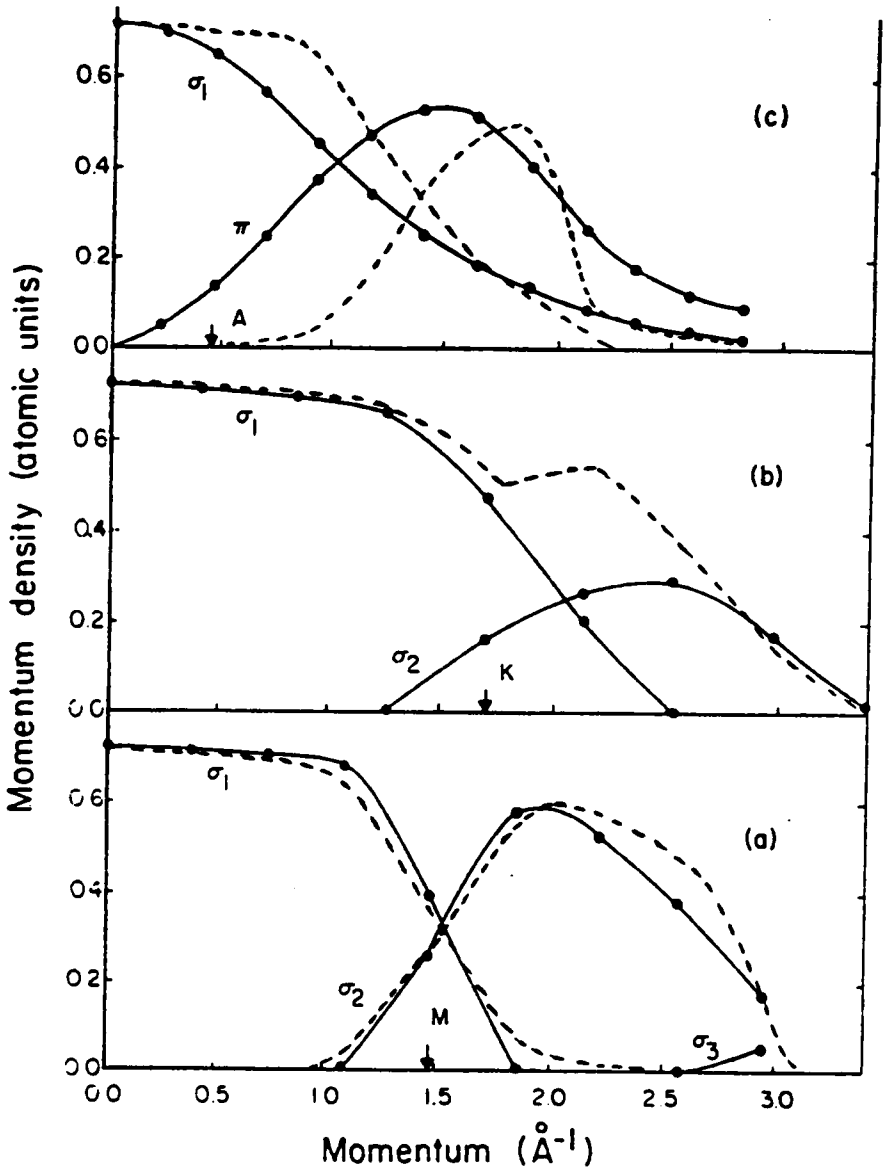


Fig. 4. Spectral momentum densities for different bands as a function of momentum; solid curves for graphite and dashed curves for diamond. (a) Momentum densities for $\sigma_1$,$\sigma_2$ and $\sigma_3$ bands for momentum in the $\Gamma \rightarrow M$ direction of graphite and $\Gamma \rightarrow L$ direction of diamond. Momentum density of the $\pi$ band is zero by symmetry. (b) Momentum densities of the $\sigma_1$ and $\sigma_2$ bands for momentum in the $\Gamma \rightarrow K$ direction of graphite and $\Gamma \rightarrow X$ direction of diamond. Momentum density of the $\pi$ band is zero by symmetry. (c) Momentum densities of the $\sigma_1$ and $\pi$ bands for momentum parallel to the c-axis ($\Gamma \rightarrow A$) of graphite, and of the $\sigma_1$ and $\sigma_2$ bands for momentum in the $\Gamma \rightarrow K \rightarrow X$ direction of diamond. Momentum densities of the $\sigma_2$ and $\sigma_3$ bands of graphite are zero by symmetry.

**Table 1. Properties of different forms of carbon. Room-temperature conductivity($\sigma_{RT}$), optical gap, density, and hardness of forms of diamond, graphite, glass carbon, evaporated a-C, ion-beam a-C, and hydrogenated a-C[64].**

| | $\sigma_{RT}$ ($\Omega^{-1}$ cm$^{-1}$) | $E_g$ (eV) | Density (g cm$^{-3}$) | Hardness (kg mm$^{-2}$) |
|---|---|---|---|---|
| Diamond | $10^{-18}$ | 5·5 | 3·515 | $10^4$ |
| Graphite | $2·5 \times 10^4$ ($\perp$c) | −0·04 | 2·267 | |
| Glassy carbon | $10^2$–$10^3$ | $10^{-2}$ | 1·3–1·55 | 800–1200 |
| Evaporated a-C | $\sim 10^{-3}$ | 0·4–0·7 | ~2·0 | 20–50 |
| Ion-beam a-C | $\sim 10^{-2}$ | 0·4–3·0 | 1·8–2·7 | |
| a-C:H | $10^{-7}$–$10^{-16}$ | 1·5–4 | 1·4–1·8 | 1250–6000 |

# III. Experiment

## 1. Experimental considerations

Our (e,2e) spectrometer has a symmetric coplanar scattering geometry. The details have been described in refs.[1,2]. The incident electron energy was 25 KeV in these measurements. For the amorphouse carbon experiment, the energy resolution was 8.6 eV FWHM and the momentum resolution was estimated to be $0.73\text{Å}^{-1}$. The measurements covered a range of momentum perpendicular to the incoming beam equal to $0 \leq |\vec{q}| \leq 3.75\text{Å}^{-1}$ The energy range was from 5.0 eV above the Fermi energy to 33.0 eV below the Fermi energy. For the graphite experiment, the energy resolution was 8.6 eV FWHM and the momentum resolution was estimated to be $0.47\text{Å}^{-1}$ and $0.73\text{Å}^{-1}$ for momentum parallel and perpendicular to the c-axis, respectively. The c-axis was perpendicular to the incoming beam. The measurements covered a range of momentum parallel to the c-axis equal to $0 \leq |\vec{q}| \leq 1.84\text{Å}^{-1}$ and a range of momentum perpendicular to the c-axis equal to $0 \leq |\vec{q}| \leq 2.35\text{Å}^{-1}$. The energy range spanned the valence band of graphite from 4.4 eV above the Fermi energy to 27.6eV below the Fermi energy. The band structure $E(\vec{k})$[3] and spectral density $|U_{\vec{K}}(\vec{G})|^2$ have been calculated from first-principles using a self-consistent,

density functional theory. The comparison between our measurements and the theoretical calculation of the spectral density provides evidence to verify the assumptions and approximations in the derivation of the (e,2e) cross section and also demonstrates whether (e,2e) spectroscopy gives sensible results when applied to a system which is well characterized. This is a crucial question to determine whether the (e,2e) technique can or can not be extended to other materials, such as amorphous solids, where the electronic structure is less well understood.

The coincidence experiment of (e,2e) is time consuming. It requires weeks even months of data taking. We took data over a four month period for the graphite measurements, for example. There are several sources of systematic errors which can arise over such a long collection time. We have considered 1) the incident electron current will vary, 2) the electron optics will vary affecting the incident current and the transmission of scattered electrons from the target to the detector, 3) high frequency noise on the power or ground lines will produce bursts of false coincidence events, 4) the sample will change with time. The variation in beam current and tune conditions is mitigated by sweeping through a set of energy-momentum values in a period which is shorter than the drift time of the system. The energy-momentum set is swept repetitively in random order under computer control. After approximately nine hours a computer file is created which stores the coincidence data, and other information, for that period of time. Then all counters are cleared and the process starts again. If there is evidence of false coincidence events in the file (the coincidence count more than ten standard deviations from the average), due, for example, to high frequency noise triggering the counter, then the file is rejected. Out of 174 files, we have rejected 6 in the graphite experiment. We monitor whether the sample is changing during the experiment by comparing files taken at the beginning of the run with files taken at the end. We saw no evidence of time dependence in the data. Finally, we took data in overlapping regions of binding energy and momentum rather than attempting to measure the total energy-momentum set in one block. This allowed us to monitor the experiment better and meant that complete data for some energy-momentum values would still exist if the ex-

periment aborted unexpectedly (the sample breaking, for example). The first set of data was taken on a coarse grid of momentum points, but spanned all the energy values. Then the other momentum columns were filled in. To normalize the data properly, we overlapped the later data sets with at least one momentum column from the first set. The ratio of the coincidence counts in the overlapping momentum columns was used as the normalizing factor.

The maximum coincidence rate we observed was $\simeq$0.02 counts/second for total momentum approximately zero and binding energy $\simeq$20 eV. We find that multiple scattering is a major factor in determining the maximum rate. Coincidence events are removed from a particular energy-momentum bin by small-angle scattering (typically creation of a plasmon) either before or after the wide angle (e,2e) collision. The optimum film thickness to maximize the coincidence rate is $\lambda/2.7$ which can be derived by maximizing $C_{000}$ with respect to $\Delta/\lambda$ ( see appendix B ) where $\lambda$ is the total mean free path of the incident electron. In the analysis of multiple scattering in our graphite data we found that the ratio of thickness to mean free path was 0.5. The coincident count rate would have been roughly 50% higher if the sample thickness of graphite had been optimum.

## 2. Sample preparation and characterization

The ion sputtered amorphous carbon films were from Aluminum Company of America. One was made using low RF power (200 W), referred to as the low power sample. The other was made at high RF power (1000 W), referred to as the high power sample. The first conditions generally produce hard films with high resistivity while the second conditions produce softer films with low resistivity. The thickness of the film is about 157 Å for the high power sample and about 144 Å for the low power sample. The TEM measurements show that our

samples have the diffused diffraction ring which prove the amorphous nature of our ion sputtered carbon samples.

The sample for the graphite experiment was natural graphite from the mines at Ticonderoga, New York. It is a hard task to prepare crystal samples for (e,2e) analysis since the thickness of sample should be less than one electron mean free path at half incident energy ( typically $\sim 150$Å ). Initial thinning of this layered material was by the "standard Scotch-tape method". Layered materials have a sheet-like structure. Therefore the layers can be pulled apart with pieces of cellophane. Successive applications of this results in a thin film ( $\sim 1000$Å ). We were not able to obtain usable samples less than 500Å thick by this procedure. In order to reduce the thickness to 100Å we took samples which were 1000 Å thick and thinned them further by reactive ion etching using a mixture of oxygen and argon at the National Research and Resource Facility for Submicron Structures(NRRFSS). In principle the carbon is chemically etched by oxygen to form an oxide loosely bound to the surface and the argon physically knock off the oxide from the surface. There is evidence that plasma etching does far less damage to the surface layers of a crystal than ion milling [40]. We obtained an area of film, slightly larger than the area of our electron beam spot ($\sim 3mm$), which we estimated was 150Å thick based on the attenuation of a laser beam passing through the sample. From an analysis of the multiple scattering contribution to our elastic scattering data (described in appendix A) we found the thickness was 110Å in rough agreement with the estimate by laser beam attenuation. The technique for preparing the film assured that the c-axis was perpendicular to the film surface. We attempted to measure the orientation of the crystal axes in the plane of the film by LEED, but were not successful due to the requirement of high temperature treatment for graphite surface. This is not too significant because with our present resolution the predicted variation in the spectral density for different momentum directions in the basal plane can not be resolved.

In order to evaluate how much damage was done to the crystal by our thinning procedure, the Raman spectra of the sample were measured before and after etching it. We also checked the spectra after taking data for several weeks to see if the sample had been ad-

versely affected by the electron beam. In Fig. 5(a) is the spectra of pristine graphite which exhibits a single Raman line at 1575 $cm^{-1}$. After thinning sample with tape (Fig. 5(b)) and etching the sample (Fig. 5(c)), the 1575 line is still present and has not broadened. A new line at 1355 $cm^{-1}$ is present which has been observed by others in microcrystalline graphite and arises from the breakdown of the k-selection rule as the crystallite size gets smaller [94-97]. It has been observed that the relative intensity of the 1355 line with respect to the 1575 line varies inversely with the planar dimension of the crystallite. The small peak at $\sim 1622 cm^{-1}$ has been associated with weak disorder in the crystallite. In Fig. 5(d) is the Raman spectra of a sample after taking (e,2e) data for five weeks. There is no visible change in the spectra. Finally, in Fig. 5(e) is the Raman spectra of amorphous carbon. It is clear that our sample has retained crystalline order through the process of thinning it.

# 3. Experimental results for graphite

The coincidence rate as a function of binding energy (with respect to the Fermi energy) for total momentum approximately equal to zero is shown in Fig. 6. The open circles are the raw data. Statistical error bars for one binding energy are shown. The coincidence rate goes to zero above the Fermi energy, but does not go to zero below the bottom of the valence band ($E_B \sim 20$ ev) because of multiple scattering. A general procedure for deconvoluting the contributions of multiple scattering from the raw data has been given by Jones and Ritter[101]. Specific application of this procedure to graphite, which is complicated by the crystalline anisotropy, is discussed in appendices. The solid circles in Fig. 6 are the deconvoluted (e,2e) scattering rate. A weak peak at $\sim$ 8 eV and a more intense peak at $\sim$ 20 eV are clearly evident. The complete set of deconvoluted data is shown in Figs. 7(a) and 7(b). In Fig. 7(a) data is shown for the momentum vector in the basal plane and with the magnitude of the momentum ranging from $-0.35 Å^{-1}$ to $2.35 Å^{-1}$ in steps of

$0.3Å^{-1}$. The component of momentum parallel to the c-axis was nominally zero, but due to a misalignment of the spectrometer, the parallel offset was $-0.61Å^{-1}$. In Fig. 7(b) data is shown for the momentum vector parallel to the c-axis from $-0.61Å^{-1}$ to $1.84Å^{-1}$ in steps of $0.27Å^{-1}$. Again, the perpendicular component of momentum was not zero, but was offset by $-0.35Å^{-1}$ because of misalignment. The solid lines in Figs. 7(a) and 7(b) are generated by fitting one or two gaussian peaks to the data with the center and amplitude of the gaussians as free parameters. The width of the gaussian peaks was determined from the data near zero momentum. The momentum dependence of the width is negligible. In Table 2 and Table 3 are the resulting parameters for momentum parallel and perpendicular to the c-axis, respectively. These results will be compared to theory in the next chapter.

# *4. Experimental results for ion sputtered a-C*

Our experimental results are shown in Figs. 8 and 9. The coincidence rate as a function of binding energy (with respect to the Fermi energy) for total momentum approximately equal to zero is shown in Fig. 8 for the high power sample. The triangles are the raw data. Statistical error bars for one binding energy are shown. The coincidence rate goes to zero above the Fermi energy, but does not go to zero below the bottom of the valence band ($E_B \sim 20$ ev) because of multiple scattering. The deconvoluting procedure for multiple scattering is described in refs. [2,101] except that for better modeling we have used a Lorentizan distribution, instead of a Gaussian distribution, for the energy resolution of our spectrometer. The parameters for the deconvolution are given in Appendix A. The stars in Fig. 8 are the deconvoluted (e,2e) scattering rate. A weak peak at $\sim$ 8 eV and a more intense peak at $\sim$ 20 eV are clearly evident. The complete set of deconvoluted data is shown in Figs. 9(a) and 9(b) for the high power and low power samples, respectively. In Fig. 9(a), data for the high power sample is shown for the momentum vector perpendicular

to the electron beams and with the magnitude of momentum ranging from $-2.75\text{Å}^{-1}$ to $-.75\text{Å}^{-1}$ in steps of $1.0\text{Å}^{-1}$ and from $-0.75\text{Å}^{-1}$ to $3.75\text{Å}^{-1}$ in steps of $0.5\text{Å}^{-1}$. In Fig. 9(b), data for the low power sample is shown for the momentum vector perpendicular to the electron beams and with the magnitude of momentum ranging from $-3.25\text{Å}^{-1}$ to $-1.25\text{Å}^{-1}$ in steps of $1.0\text{Å}^{-1}$ and from $-1.25\text{Å}^{-1}$ to $3.25\text{Å}^{-1}$ in steps of $0.5\text{Å}^{-1}$. The component of momentum parallel to the incoming electron beam was nominally zero, but due to a misalignment of the spectrometer, the parallel offset was $-0.4\text{Å}^{-1}$ in both cases.

The solid lines in Figs. 9(a) and 9(b) are generated by fitting two Lorentzian peaks to the data. The standard least square method is employed. It is clear that two peaks are resovled in our data when $q \leq 1.75\text{Å}^{-1}$. When $q > 1.75\text{Å}^{-1}$ our resolution can not resolve the peaks. There are three free parameters, peak position, width and amplitude, for each Lorentzian peak. Thus six free parameters are in our fitting. In order to reduce the number of free parameters, we choose the position of the two peaks from viewing the data and then let the computer program searches for the other four parameters based on the least square fitting. For the bottom peaks, the resulting width fluctuated $\sim 1$ eV around 8 eV as a function of momentum for $q \leq 1.75\text{Å}^{-1}$; for the top peaks the resulting width also fluctuated $\sim 1$ eV around 6.6 eV as a function of momentum for $q \leq 1.75\text{Å}^{-1}$. These results indicate that the widths do not depend on momentum within our experimental resolution. Then the fitting procedure is run again using the average widths of 8 eV and 6.6 eV for the bottom and top peaks, respectively, and letting the computer program search for peak positions and amplitudes. We used two peaks with the above two widths to fit the single broader peak of our data for $q > 1.75\text{Å}^{-1}$ based on the consideration that the width should not jump discontinuously. In Table 4 and Table 5 are the resulting parameters for the high power sample data and the low power sample data, respectively. These results will be discussed in the next chapter.

In order to get some feeling about the true peak width in the amorphous phase without resolution broadening, we have done the following simulation. We convolute a $\delta$ function with the smearing function for amorphous carbon using the parameters in Appendix A. Then

we deconvoluted the resulting function by the methods used for the a-C data exactly(the same number of iterations and the same deconvoluting range). We would get zero width for the simulation peak after deconvolution if both the deconvoluting range and the number of iterations were infinite. In practice, we use a finite number of iterations and finite energy range so that the resulting width is only a little bit less than the resolution of the experiment. The resulting width for the simulation peak is $\sim$ 6 eV which is about 2 eV narrower than the width of the bottom peaks and 0.6 eV narrower than the top peaks. The additional width in the experimental data may arise from the broadening of the electron states in the amorphous phase or may be due to noise of our data. It is too ambitious to make any conclusion at this point because our resolution is 8.6 eV.

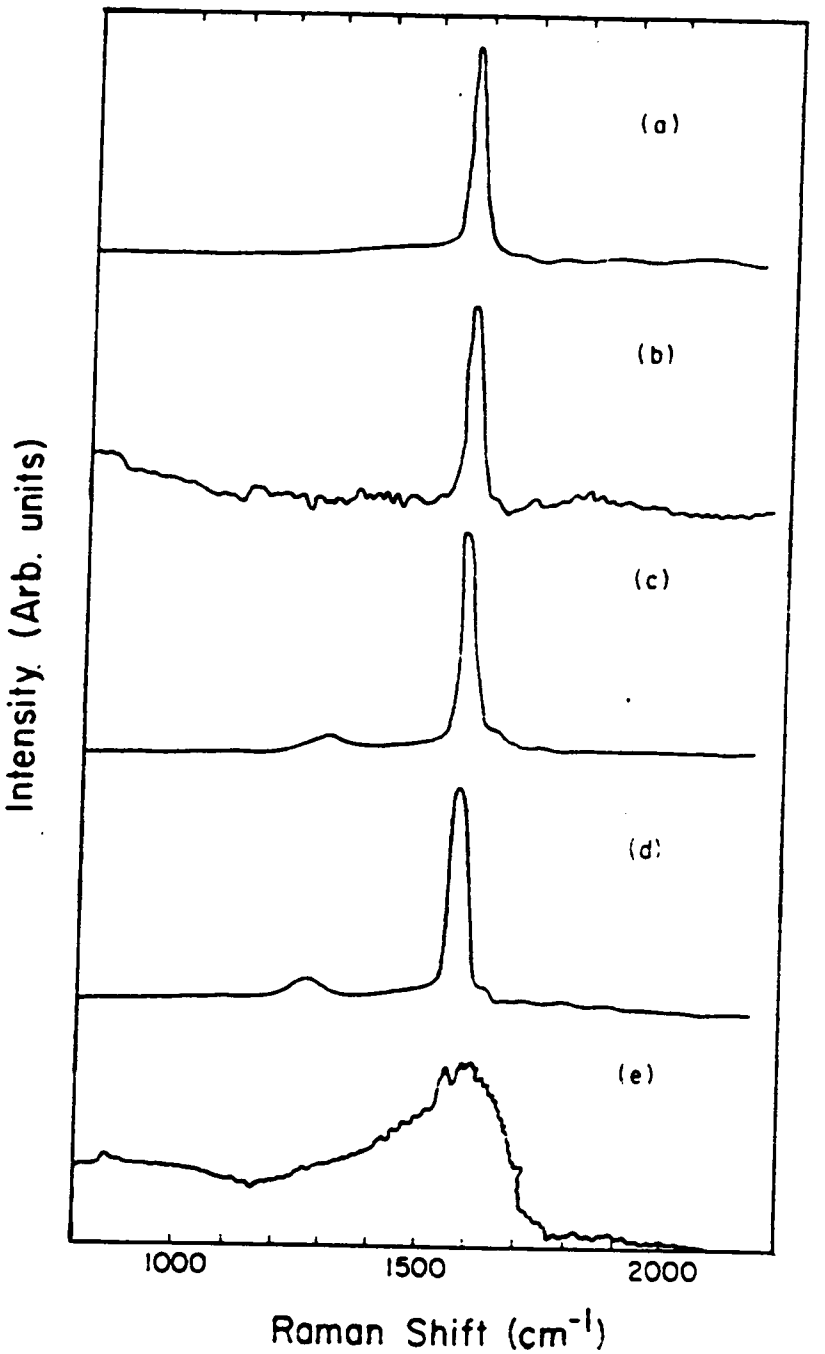


Fig. 5. Raman spectra of our samples and of amorphous carbon. (a) Raman spectra of graphite crystal. (b) Raman spectra of graphite film after thinning with scotch tape. (c) Raman spectra of graphite film after thinning with scotch tape and with reactive ion etching. (d) Raman spectra of graphite film after electron bombardment for five weeks. (e) Raman spectra of amorphous carbon.

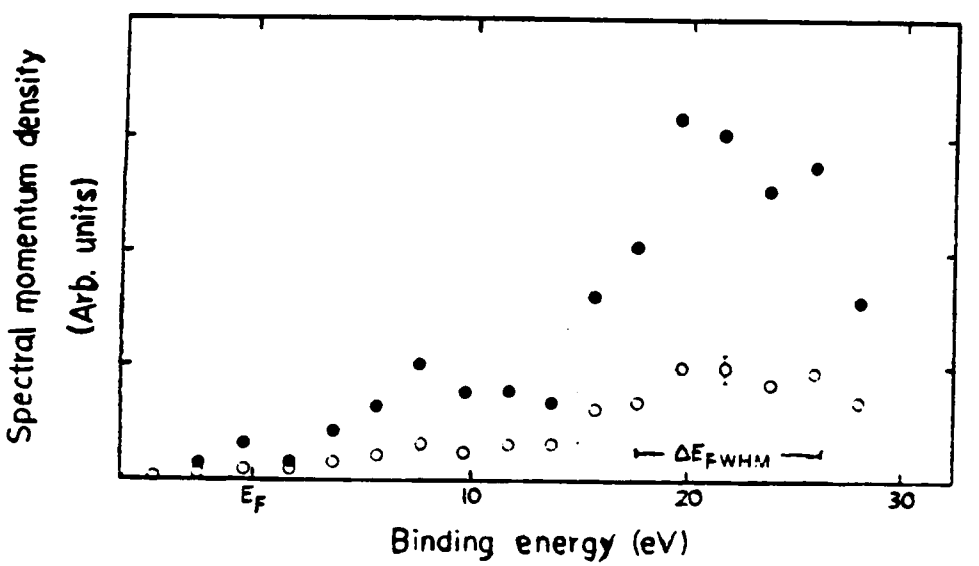


Fig. 6. The experimental spectral momentum density of graphite. The spectral momentum density as a function of energy (with respect to the Fermi energy) with the component of momentum parallel to the c-axis equal to $0.21\text{Å}^{-1}$ and with the component of momentum perpendicular to the c-axis equal to $-0.35\text{Å}^{-1}$. The open circles are the raw data. The closed circles are the data after correcting for multiple scattering.

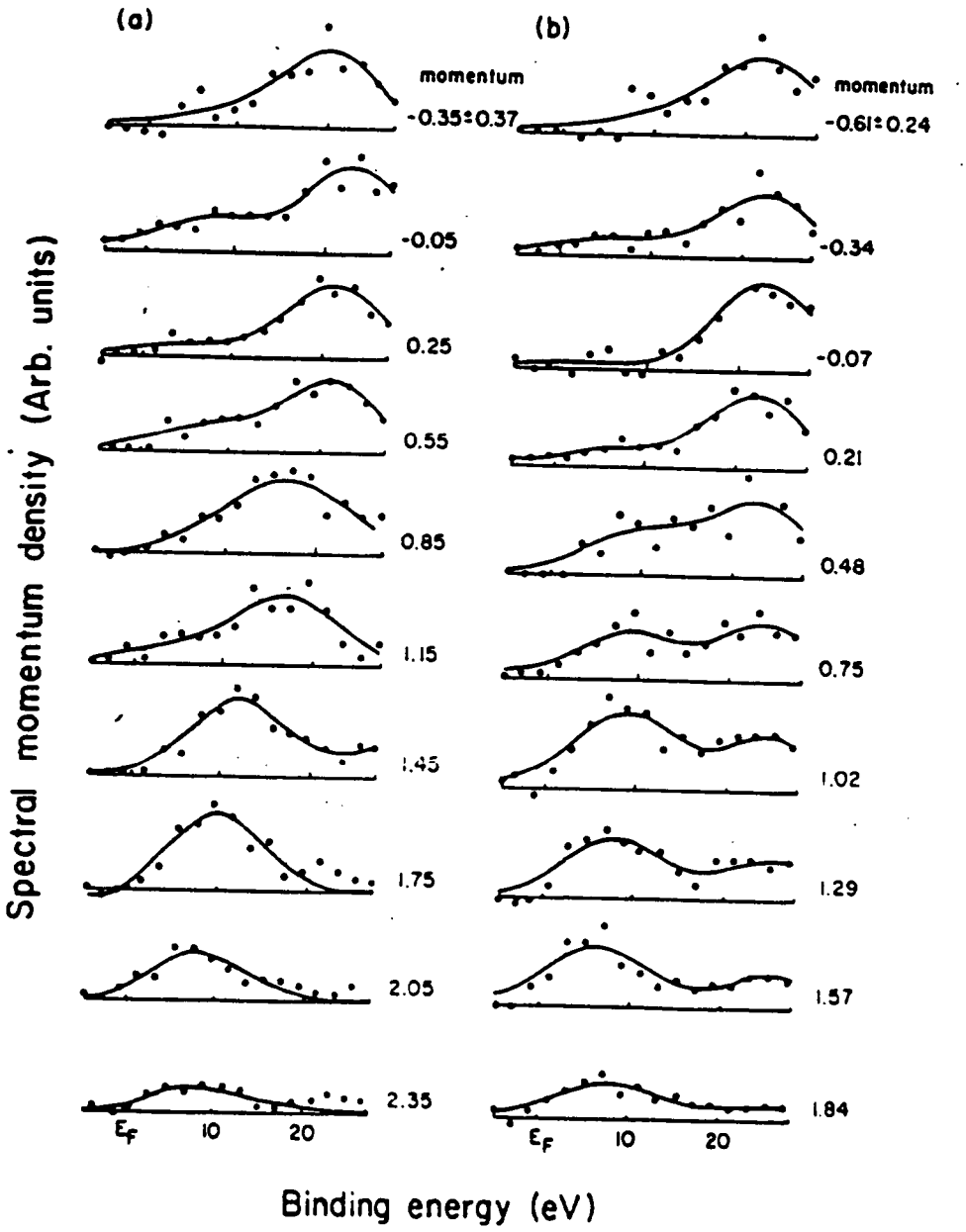


Fig. 7. The deconvoluted spectral momentum densities of graphite. The spectral momentum densities as a function of energy (with respect to the Fermi energy) for different momentum. The solid lines are least square fits of gaussian peaks to the data. (a) Momentum perpendicular to the c-axis (parallel component = $-0.61\text{Å}^{-1}$) . (b) Momentum parallel to the c-axis (perpendicular component = $-0.35\text{Å}^{-1}$).

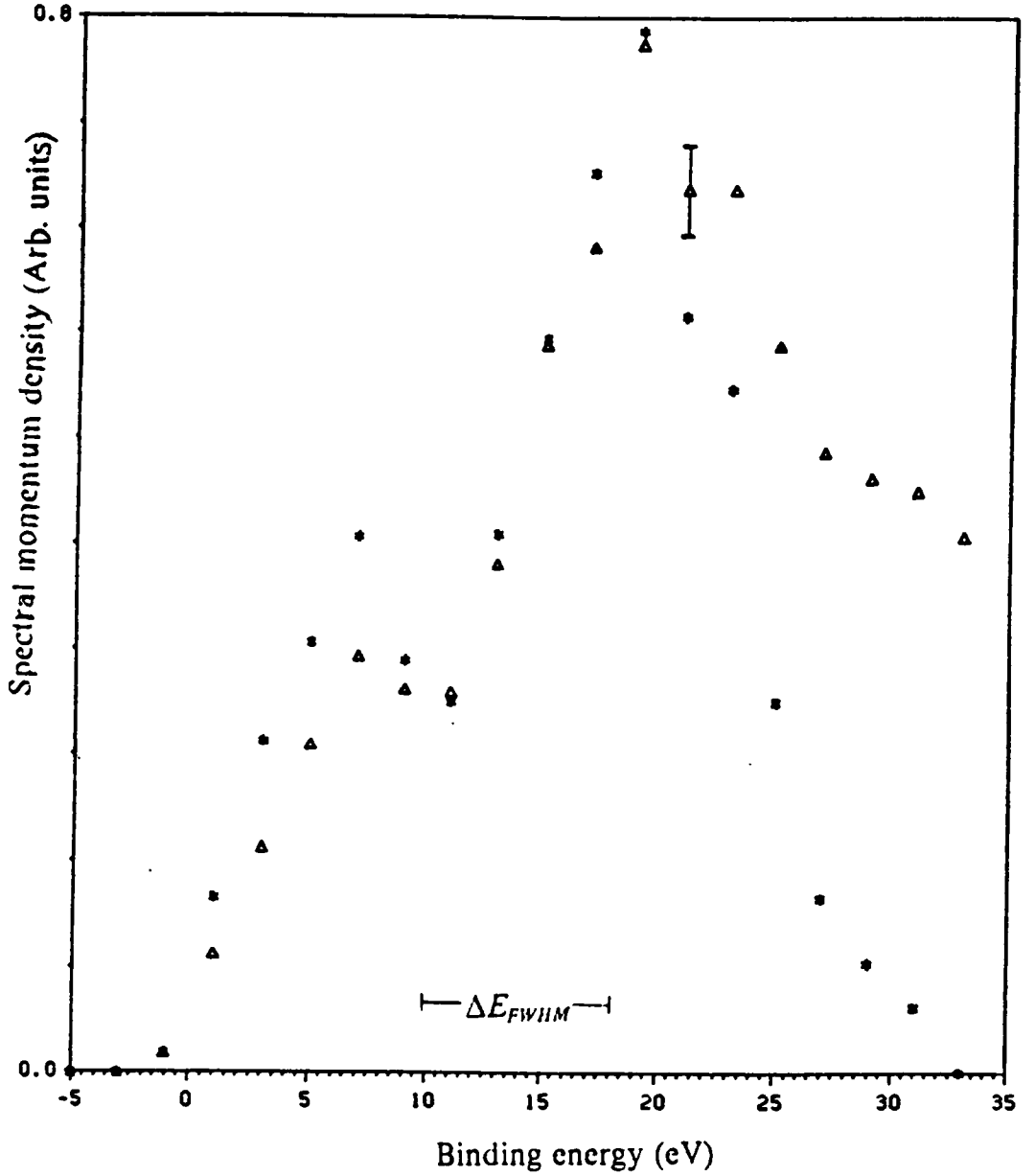


Fig. 8. The experimental spectral momentum density of ion sputtered a-C. The spectral momentum density of high power ion sputtered a-C as a function of energy (with respect to the Fermi energy) with the component of momentum parallel to the incoming electron beam equal to $-0.4\text{Å}^{-1}$ and with the component of momentum perpendicular to the incoming electron beam equal to $-0.25\text{Å}^{-1}$. The triangles are the raw data. The stars are the data after correcting for multiple scattering.

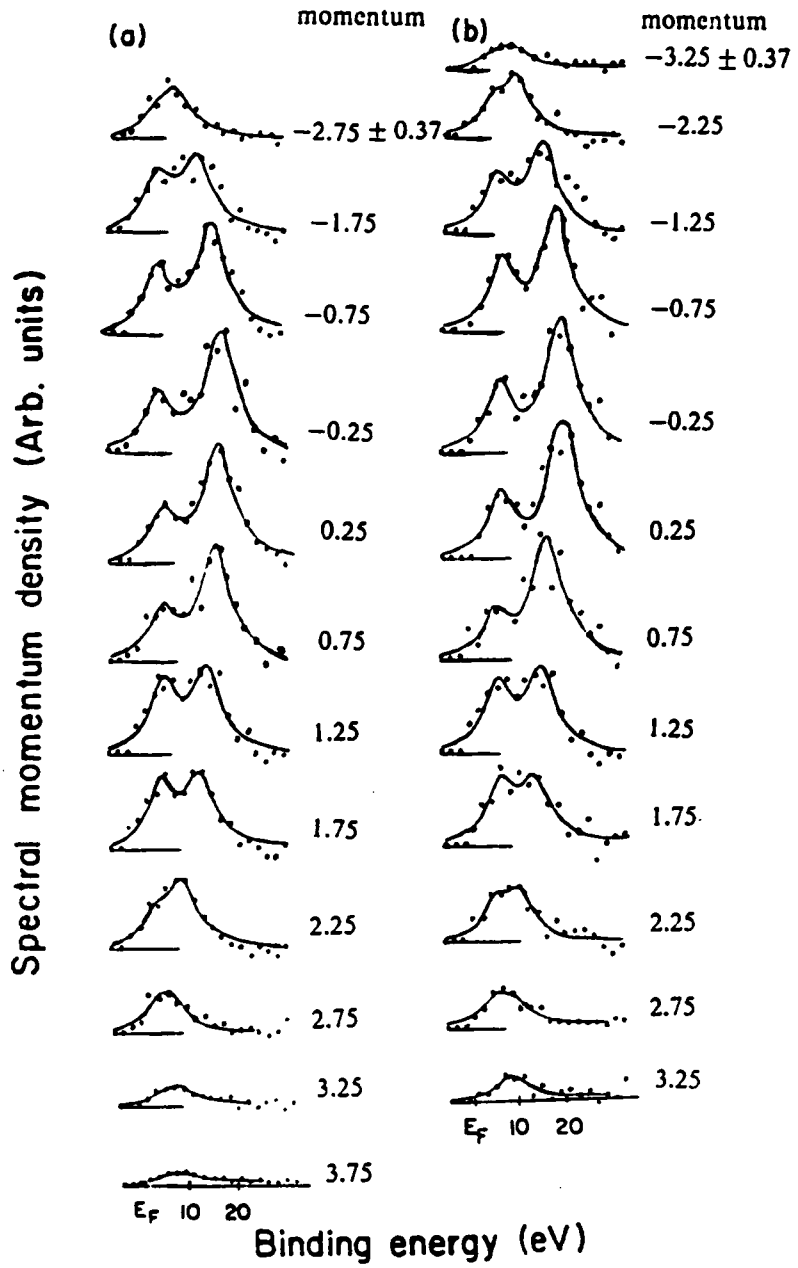


Fig. 9. The deconvoluted spectral momentum densities of ion sputtered a-C. The spectral momentum densities of two ion sputtered a-C samples as a function of energy (with respect to the Fermi energy) for different momentum. The solid lines are least square fits of Lorentzian peaks to the data. (a) High power sample (the component of momentum parallel to incoming electron beam = $-0.4\text{Å}^{-1}$) . (b) Low power sample (the component of momentum parallel to incoming electron beam = $-0.4\text{Å}^{-1}$) .

**Table 2. Fitting parameters for graphite(momentum parallel to the c-axis with perpendicular component = -0.35 $Å^{-1}$ )**

| $q(Å^{-1})$ | *Energy (ev) first peak* | *Amplitude first peak* | *Energy (ev) second peak* | *Amplitude second peak* |
|---|---|---|---|---|
| -0.61 ± 0.24 | 10.65 | 0.12 | 22.3 | 0.56 |
| -0.34 | 6.06 | 0.11 | 20.9 | 0.47 |
| -0.07 | 2.94 | 0.04 | 22.5 | 0.67 |
| 0.21 | 6.53 | 0.10 | 22.1 | 0.53 |
| 0.48 | 9.79 | 0.31 | 22.9 | 0.53 |
| 0.75 | 9.21 | 0.32 | 24.5 | 0.42 |
| 1.02 | 9.32 | 0.55 | 25.3 | 0.40 |
| 1.29 | 8.60 | 0.44 | 25.4 | 0.31 |
| 1.57 | 6.85 | 0.42 | 26.2 | 0.23 |
| 1.84 | 8.48 | 0.25 | 25.5 | 0.09 |

**Table 3. Fitting parameters for graphite(momentum perpendicular to the c-axis with parallel component = -0.61 $Å^{-1}$ )**

| $q(Å^{-1})$ | *Energy (ev) first peak* | *Amplitude first peak* | *Energy (ev) second peak* | *Amplitude second peak* |
|---|---|---|---|---|
| -0.35 ± 0.37 | 7.10 | 0.08 | 20.1 | 0.57 |
| -0.05 | 7.49 | 0.19 | 23.0 | 0.60 |
| 0.25 | 6.00 | 0.09 | 21.4 | 0.53 |
| 0.55 | 7.71 | 0.16 | 21.3 | 0.50 |
| 0.85 | 12.50 | .26 | 19.3 | 0.37 |
| 1.15 | 4.64 | 0.12 | 17.2 | 0.48 |
| 1.45 | | | 12.1 | 0.55 |
| 1.75 | | | 9.20 | 0.62 |
| 2.05 | | | 7.18 | 0.40 |
| 2.35 | | | 8.53 | 0.19 |

**Table 4. Fitting parameters for high power ion sputtered a-C**

| $q(Å^{-1})$ | *Energy (ev) first peak* | *Amplitude first peak* | *Energy (ev) second peak* | *Amplitude second peak* |
|---|---|---|---|---|
| -2.75 ± 0.37 | 3.41 | 0.0345 | 8.62 | 0.128 |
| -1.75 | 5.50 | 0.120 | 13.81 | 0.198 |
| -0.75 | 6.51 | 0.132 | 18.33 | 0.284 |
| -0.25 | 5.92 | 0.123 | 19.61 | 0.319 |
| 0.25 | 6.45 | 0.106 | 18.59 | 0.312 |
| 0.75 | 6.55 | 0.113 | 18.20 | 0.307 |
| 1.25 | 7.01 | 0.151 | 16.28 | 0.222 |
| 1.75 | 5.99 | 0.136 | 14.58 | 0.186 |
| 2.25 | 4.59 | 0.065 | 10.63 | 0.171 |
| 2.75 | 3.70 | 0.031 | 7.27 | 0.095 |
| 3.25 | 4.02 | 0.018 | 8.39 | 0.046 |
| 3.75 | 4.30 | 0.0098 | 8.74 | 0.029 |

**Table 5. Fitting parameters for low power ion sputtered a-C**

| $q(Å^{-1})$ | *Energy (ev) first peak* | *Amplitude first peak* | *Energy (ev) second peak* | *Amplitude second peak* |
|---|---|---|---|---|
| -3.25 ± 0.37 | 4.50 | 0.024 | 9.40 | 0.64 |
| -2.25 | 5.00 | 0.070 | 10.25 | 0.168 |
| -1.25 | 6.02 | 0.138 | 15.80 | 0.268 |
| -0.75 | 7.96 | 0.176 | 19.60 | 0.353 |
| -0.25 | 7.90 | 0.166 | 21.15 | 0.392 |
| 0.25 | 7.90 | 0.156 | 21.50 | 0.395 |
| 0.75 | 6.98 | 0.109 | 17.98 | 0.355 |
| 1.25 | 7.03 | 0.136 | 17.70 | 0.291 |
| 1.75 | 7.01 | 0.162 | 14.34 | 0.185 |
| 2.25 | 5.99 | 0.089 | 11.1 | 0.136 |
| 2.75 | 5.00 | 0.054 | 9.00 | 0.075 |
| 3.25 | 6.50 | 0.014 | 8.47 | 0.066 |

# IV. Discussion and Conclusion

## *1. Discussion of graphite*

Our data is compared with theory in Figs. 10 and 11 for momentum parallel and perpendicular to the c-axis, respectively. There is one free parameter for matching experiment and theory which is an overall scale factor. This factor has been determined from the average spectral density near $q = 0$ ($q \leq 0.5\text{Å}^{-1}$of the $\sigma_1$ band). The same scale factor is applied to all the data, for momentum both parallel and perpendicular to the c-axis. In the first case, Fig. 10, there is a constant component of momentum perpendicular to the c-axis, $q_{P_\perp} = -0.35\text{Å}$, while the component of momentum parallel to the c-axis is variable. The theoretical $\pi$-band (dashed line) and $\sigma_1$ band (solid line), almost dispersionless along the c-axis, are drawn in the repeated zone representation. The dispersion is $\leq$ 1 eV and has not been shown since it can not be observed with our energy resolution. The first Brillouin zone boundary for momentum parallel to the c-axis is $q_{P_\parallel} = 0.47\text{Å}^{-1}$ . We represent the spectral momentum density as an arrow on the energy-momentum plane. The theoretical densities are light arrows on top of the band dispersion; the experimental results from Table 2 are the heavy arrows. The agreement between theory and experiment is ex-

cellent for the $\pi$ band. The spectral density of the $\sigma_1$ band agrees very well with theory; the apparent dispersion of the band to larger binding energy is probably due to incomplete deconvolution of multiple scattering from the data. The spectral momentum densities of the two less tightly bound sigma bands, $\sigma_2$ and $\sigma_3$, are zero for symmetry reasons.

The spectral densities as a function of momentum perpendicular to the c-axis are shown in Fig. 11. In this case there is a constant component of momentum parallel to the c-axis $q_{P_e} = -0.61\text{Å}$ . Again the theoretical density is represented by the light arrows placed on the energy dispersion curves, while the experimental results from Table 3 are represented by heavy arrows. There is very good agreement between theory and experiment for the $\sigma_1$ band. The spectral densities of $\sigma_2$ bands are predicted to be negligible in the first Brillouin zone, then rise sharply at the zone boundary and peak in the second Brillouin zone. For $q \leq 1\text{Å}^{-1}$ we can not resolve the $\pi$, $\sigma_2$ and $\sigma_3$ bands because of our low resolution. We tentatively identify the weak structure at $q = 0.25\text{Å}^{-1}$ (E = 6 eV), $q = 0.55\text{Å}^{-1}$ (E = 7.7 eV) and $q = 1.15\text{Å}^{-1}$ (E = 4.6 eV) with the $\pi$ band. The existence of $\pi$ band spectral density is due to the small component of momentum parallel to the c-axis. The data at $q = 0.85\text{Å}^{-1}$ can be fit almost equally well with two Gaussians centered at E = 12.5 eV and E = 19.3 eV (as plotted on Fig. 11) or with one Gaussian at E = 15.4 eV. The first choice preserves the continuity of the spectral density in the $\sigma_1$ band but raises the question of whether the peak at E = 12.5 eV is associated with the $\sigma_2$ band. If it is, then the spectral density of the $\sigma_2$ band in the first Brillouin zone is much larger than predicted by theory. But this possible discrepancy is tentative until the measurement can be repeated with better resolution. In Fig. 11 we have compared our data to the calculated spectral density for momentum in the $\Gamma \rightarrow M$ direction. Within our resolution and statistics, the difference in spectral density for different directions in the basal plane can not be resolved.

# 2. Discussion of ion sputtered a-C

There are three primary aspects to be discussed in this section. First, we will discuss the "band structure", sum rules, and the discrepancy between our result and that of Savvide. Secondly, we will compare the spectral momentum densities with those of an angular average of graphite. Finally, we will propose a new hybridization model to explain the discrepancy in the comparison.

## A. Band structure and sum rules

The "band structure" of ion sputtered carbon can be obtained by projecting the peak position and amplitude of our data onto the (E,q) plane. The results are shown in Fig. 12. The arrows and the dashed arrows are spectral momentum densities from Table 4 and Table 5 for the high power and the low power sample, respectively. The scale factor for each set of data has been determined from a model which will be discussed next. The band width is about 16.5 eV, while the band width is 21 eV for diamond and 20 eV for graphite. There is a band around 8 eV which is remarkably similar to the $\pi$ band of graphite. Figs. 9 and 12 show that there is no difference between the spectral momentum densities of the high power and the low power samples within our resolution and statistics.

As discussed in chapter II, the existence of a distinct graphitic phase interspersed in a diamondlike medium and vice versa has been proposed[79,82,86,89,91] for ion sputtered a-C. Recently, based on EELS and optical data, Fink et al.[70,71] and Savvides[22,23] estimated the proportion of $sp^3$ bonding in a-C by using sum rules.

Sum rules have been discussed in detail by Wooten[98]. For solids, there are two sum rules which are analogous to the sum rule $\sum_m f_{mn} = Z$ for atoms. One is

$$\int_0^\infty \omega\, \varepsilon_2(\omega) d\omega = \frac{1}{2}\pi\, \omega_P^2$$

which is related to the rate of energy absorption by transverse fields (photons) and hence is related to interbands transitions. The plasma frequence is $\omega_P = 4\pi N_a Z e^2/m$ where $N_a$ is the density of atoms. Another is

$$\int_0^\infty \omega\, Im \frac{-1}{\varepsilon(\omega)}\, d\omega = \frac{1}{2}\pi\, \omega_P^2$$

which is related to plasma excitations by longitudinal fields (electrons). Sum rules are frequently defined in terms of an effective number of electrons per atom, $n_{eff}$, contributing to the optical properties over a finite energy range. Thus

$$\int_0^E E'\, \varepsilon_2(E') dE' = \frac{1}{2}\pi\, (4\pi N_a e^2/m)\hbar^2\, n_{eff}(E)$$

and

$$\int_0^E E'\, Im \frac{-1}{\varepsilon_2(E')}\, dE' = \frac{1}{2}\pi\, (4\pi N_a e^2/m)\hbar^2\, n_{eff}(E)$$

One thing must be noted that these two sum rules give different values for $n_{eff}$ for small $E$, but the same values for large enough $E$ ( larger than the plasma energy ) because of the different origin of the sum rules[99,100].

In applying the first sum rule, Savvides argued that the $\pi \rightarrow anti\ \pi$ transitions are exhausted at 9 eV from energy-band calculations and detailed optical spectra of graphite. Since one electron per carbon atom is available for $\pi$ bonding, the effective number, $n_{eff}$, for graphite increases with photon energy to a value of 1 at about 9 eV. At this energy, the

$\sigma \rightarrow anti\ \sigma$ begins and leads to $n_{eff}$ rising rapidly with energy and asymptotically to a value of 4. In diamond, the $\sigma \rightarrow anti\ \sigma$ transitions are zero before 7 eV from energy-band calculations(about 5 eV band gap) and therefore $n_{eff} = 0$ for energies up to 7 eV and it rises sharply above 7 eV. Briefly, since most $\pi$ electrons in graphite make their contribution to $n_{eff}$ below 9 eV, and no electrons in diamond make contribution to $n_{eff}$ before 7 eV, therefore Savvides and Fink et al. argued that it is possible to determine $C_{sp2}$, the concentration of threefold coordinated carbon atoms using their data(see Fig. 13). $C_{sp2}$ is simply equal to the ratio of $n_{eff}$ for a-C films to $n_{eff}$ for graphite at 7 eV. Subtracting $C_{sp2}$ from unity yields $C_{sp3}$, the concentration of fourfold coordinated carbon atoms. In this way, Savvides and Fink et al. conclude that there is almost no $sp^3$ bonding in evaporated a-C, and there can be as high as 75 % $sp^3$ bonding in ion sputtered a-C depending on the film making power.

In their analyses, Savvides[22,23] and Fink et al.[70,71] assumed that a-C has a band structure consisting of two parts. One is the pure band structure of graphite and the other one is the pure band structure of diamond. From Chapter II we know that the momentum density of $\pi$ electrons in graphite peaks around $q = 1.5\text{Å}^{-1}$, and the vertical $\pi$-$anti\ \pi$ splitting at $\vec{q} = 1.5\text{Å}^{-1}$ is less than 9 eV. There is negligible momentum density of $\pi$ electron near $q = 0.\text{Å}^{-1}$ where the $\pi$- $anti\ \pi$ splitting is larger than 9 eV. Of course, there are no transitions in diamond for energy less than 7 eV, because there is no state within this range of energy for $\sigma$ electrons making transitions (band gap is about 5 eV). Thus, based on the assumption that the band structure of a-C is simply a linear combination of the graphite and diamond band structure, Savvides and Fink et al. can separate $\pi$ transitions from $\sigma$ transitions, and therefore determine $C_{sp2}$ and $C_{sp3}$.

Unfortunately, our results show that the "band structure" in a-C is different from that in graphite or diamond (see Fig. 12). The momentum density of the $\pi$ band is significantly different from that of graphite. The momentum density of $\pi$ band is nearly constant from $q = 0$ to $q \simeq 2.0\text{Å}^{-1}$, with a binding energy of about 8 eV. That is, the $\pi$ electrons near $q = 0\text{Å}^{-1}$ make significant contribution to $\pi$ transitions, requiring energy up to about 16 eV. And also because the $\pi$ band has been flattened up to $q \simeq 2.0\text{Å}^{-1}$, the $\pi$ transitions for

$q < 2.0\text{Å}^{-1}$ require about 15 eV energy, if we assume that the *anti* $\pi$ band also has been flattened in the same way. Even if we assume the *anti* $\pi$ band is the same as in graphite the $\pi$ transition still requires a larger energy than that in graphite because of the flattening of the $\pi$ band. These two factors imply that the oscillator strength for the $\pi - anti\ \pi$ transitions is not exhausted by 8 or 9 eV as Savvides and Fink et al. assume, but saturates at energies > 12eV and cannot be separated from $\sigma$ transitions. Assuming that the oscillator strength saturates at ~ 8eV will result in an estimate for $C_{sp^2}$ in a-C which is too small and in turn to predict $sp^3$ which is too large. These are qualitative arguments which should be checked by calculation of the frequency dependent dielectric function $\varepsilon(\omega)$ for a-C.

From the above analyses, it is clear that the estimate of $sp^2$ and $sp^3$ of Savvides and Fink et al. in a-C is incorrect because of their assumption of a crystalline band structure for a-C, due to the lack of experimental results on the band structure for a-C. Our (e,2e) measurements provide just this information about the band structure of amorphous solids.

An estimate of the number of electrons occupying each band can also be obtained by integrating the spectral momentum density of a band over energy and momentum. It is useful to define a partial sum

$$n_\sigma(q) = \int_0^\infty \int_0^q 4\pi q'^2 \rho_\sigma(E, q') dE dq' = \int_0^q 4\pi q'^2 \rho_\sigma(q') dq' \qquad [IV.1]$$

and

$$n_\pi(q) = \int_0^\infty \int_0^q 4\pi q'^2 \rho_\pi(E, q') dE dq' = \int_0^q 4\pi q'^2 \rho_\pi(q') dq' \qquad [IV.2]$$

where $n_\sigma(q)$ and $n_\pi(q)$ are the numbers of electrons occupying, respectively, the lower and the upper band within a spherical volume of radius $q$ in the momentum space. The results are shown in Fig. 14. The pluses and the stars are the number of electrons in the bottom and the upper bands for the high power sample, respectively. The squares and the triangles are

the number of electrons in the bottom and the upper band for the low power sample, respectively. The $n_\sigma(q > 2.25\text{Å}^{-1})$ for the high power sample seems larger than that of the low power sample. This may be just an effect of our scaling procedure. As discussed in Chapter II, the spectral momentum densities of the graphite $\sigma$ bands and the lowest three diamond bands are similar up to the third Brillouin zone( $q \simeq 3.0\text{Å}^{-1}$). The spectral momentum density of the fourth diamond band is significant only in the fourth Brillouin zone. The spectral momentum density falls off like $1/q^2$ (normalization condition ) and with our statistics cannot be measured for $q \geq 4.0\text{Å}^{-1}$ . Therefore, if there were significant diamond bonding, we would not observe the fourth band.

From Chapter II we know that $n_\pi(3.0)/n_\sigma(3.0) \simeq 1/2$ for graphite. That is, within $\vec{q} = 3.0\text{Å}^{-1}$ there is one $\pi$ electron and two $\sigma$ electrons. We also know that there are two $\sigma$ electrons in diamond too, within this momentum range. That is, the ratio of $n_\pi/n_\sigma$ only depends on the amount of $\pi$ electrons. Therefore, we can estimate the amount of $sp^2$ or $sp^3$ bonding from equations IV.1 and IV.2, provided that the $sp^3$ mixing with $sp^2$ model is correct. In this way, we get $n_\pi(3.0)/n_\sigma(3.0) \simeq 0.87/2$ for the high power sample and $n_\pi(3.0)/n_\sigma(3.0) \simeq 1.11/2$ for the low power sample. That is, there is 87 % $sp^2$ or 13 % $sp^3$ bonding in the high power sample and there is 111% $sp^2$ bonding in the low power sample. Of course, it is impossible for any sample to possess more than 100 % $sp^2$ bonding. However, 11 % is within the statistis and fitting error bar in our data. Our result is definitely different from Savvides's result which shows that there is 55 % $sp^2$ bonding. This is a further evidence that the arguments of Savvides and Fink et al. for estimating $sp^3$ bonding in a-C are not correct.

## B. Comparison with an angular average of graphite

The spectral densities of the bottom and the upper bands are shown in Fig. 15 for momentum from 0. to $3.75\text{Å}^{-1}$. The pluses and the stars are momentum densities of the bottom and the upper band for the high power sample, respectively. The squares and the triangle

are momentum densities of the bottom and the upper bands for the low power sample, respectively. The wave function for the bottom band is S-like; that is, the momentum density is maximum at q=0 and decreases monotonically as q increases. The wave function for the upper band appears to be a mixture of S and P characteristics. The momentum density is finite at $q = 0$, but appears to peak at $q = 1.5\text{Å}^{-1}$. This peak is not resolved from the error bars, but the momentum density of the upper band is not consistent with a pure S or P wave function.

Based on the strained layer model of Egrun[80,85] and on the suggestion of Haydock[18], we compare our spectral momentum density with an angular average bands of graphite. In Fig. 15, the upper solid curve is the spectral momentum density of $\sigma$ bands of graphite after simple angular average. Namely,

$$\bar{\rho}_\sigma(q) = \frac{1}{3}\left[\rho_\sigma^{\Gamma-M}(q) + \rho_\sigma^{\Gamma-K}(q) + \rho_\sigma^{\Gamma-A}(q)\right] \qquad [IV.3]$$

It averages over only $\Gamma - K$, $\Gamma - M$, and $\Gamma - A$ directions since we do not have information for other directions. However, it is almost exact for $q < 1.5\text{Å}^{-1}$ because the spectral momentum density has a S-like character which does not depend closely on direction. The right side ( $q > 1.5\text{Å}^{-1}$ ) of the curve has been adjusted by the normalization condition based on the consideration that the angular average of the $\sigma$ band for this part of curve is uncertain. The lower solid curve is the spectral momentum density of the $\pi$ band of graphite after angular an average. Namely,

$$\bar{\rho}_\pi(q) = \frac{1}{4\pi}\int \rho_\pi(q,\theta)d\Omega = \frac{1}{4\pi}\int \rho_\pi(q)\,\cos^2\theta\, d\Omega = \frac{1}{3}\,\rho_\pi(q) \qquad [IV.4]$$

Here, we neglect the dispersion along the different direction since it is within our energy resolution; and $\rho_\pi(q)$ is shown in Fig. 4(c).

As Fig. 15 shows, if we scale the data for the bottom band so that it equals the theoretical density at q=0, then the spectral momentum density of the bottom band agrees well with

that of the $\sigma$ band for $q \leq 1.5\text{Å}^{-1}$. The spectral density is larger than that predicted by the theory for $q > 1.5\text{Å}^{-1}$. The spectral momentum density of the upper band does not agree with that of the theoretical $\pi$ band but the experimental results for evaporated a-C does [109]. One definite difference is that the spectral momentum density is much larger than that of graphite for $q \leq 1.5\text{Å}^{-1}$. There is no way to scale the data to make the experimental and theoretical results for the $\pi$ band agree. We propose the following model to explain this discrepancy.

## C. Hybridization model

The momentum density of the upper band appears to be an admixture of $\sigma$ band with the $\pi$ band of graphite. Namely,

$$\Phi_{\sigma}^{m}(\vec{r}) = \frac{1}{\sqrt{1+\alpha^2}} [\Phi_{\sigma}(\vec{r}) + \alpha\ \Phi_{\pi}(\vec{r})] \qquad [IV.5]$$

and

$$\Phi_{\pi}^{m}(\vec{r}) = \frac{1}{\sqrt{1+\alpha^2}} [\Phi_{\pi}(\vec{r}) + \alpha\ \Phi_{\sigma}(\vec{r})] \qquad [IV.6]$$

Here, $\Phi_{\sigma}^{m}$ and $\Phi_{\pi}^{m}$ are the wave functions for the $\sigma$ bands and $\pi$ bands after mixing, respectively. Therefore,

$$\rho_{\sigma}^{m} = \frac{1}{1+\alpha^2}\rho_{\sigma} + \frac{\alpha^2}{1+\alpha^2}\rho_{\pi} + \frac{2\alpha}{1+\alpha^2}\int \Phi_{\sigma}(\vec{r})\,\Phi_{\pi}(\vec{r'})\ e^{-i\vec{q}\cdot(\vec{r}+\vec{r'})}\ d\vec{r}\ d\vec{r'} \qquad [IV.7]$$

and

$$\rho_{\pi}^{m} = \frac{1}{1+\alpha^2}\rho_{\pi} + \frac{\alpha^2}{1+\alpha^2}\rho_{\sigma} + \frac{2\alpha}{1+\alpha^2}\int \Phi_{\sigma}(\vec{r})\,\Phi_{\pi}(\vec{r'})\; e^{-i\vec{q}\cdot(\vec{r}+\vec{r'})}\, d\vec{r}\, d\vec{r'} \qquad [IV.8]$$

Here, $\rho_{\sigma}^{m}$ and $\rho_{\pi}^{m}$ are the spectral momentum densities for the bottom and the upper bands after mixing, respectively.

As discussed in Chapter II, the spectral momentum density is the square of the wave function in momentum space. Therefore, no phase information can be obtained from our measurements. In our $\sigma - \pi$ mixing model we will neglect the cross terms in the integrals in the equations IV.7 and IV.8 or in the equations IV.5 and IV.6, since we do not know the phase of the wavefuctions. This is not a bad approximation because local symmetries minimize this term(the orbitals lie in orthogonal planes)[64]. Taking an angular average for equations IV.7 and IV.8 with the above approximation, we have

$$\rho_{\sigma}^{a} = \frac{1}{1+\alpha^2}\bar{\rho}_{\sigma} + \frac{\alpha^2}{1+\alpha^2}\bar{\rho}_{\pi} \qquad [IV.9]$$

and

$$\rho_{\pi}^{a} = \frac{1}{1+\alpha^2}\bar{\rho}_{\pi} + \frac{\alpha^2}{1+\alpha^2}\bar{\rho}_{\sigma} \qquad [IV.10]$$

Here, $\rho_{\sigma}^{a}$ and $\rho_{\pi}^{a}$ are the spectral momentum densities after the angular average for the mixing bottom and upper bands of graphite, respectively.

There are two parameters, an overall scale factor and $\alpha$, for fitting the theoretical expressions to the data. The scale factor was determined from the $\sigma$ band at $q = 0$. The scale factor and $\alpha$ were adjusted for optimum fit of the total data set. The dash curves in Fig. 16 correspond to $\alpha = 0.58 \pm 0.08$ in equations IV.9 and IV.10. That is, there are $75 \pm 5\%$ of $\rho_{\sigma}$ and $25 \pm 5\%$ of $\rho_{\pi}$ in $\rho_{\sigma}^{a}$; and there are $25 \pm 5\%$ of $\rho_{\sigma}$ and $75 \pm 5\%$ of $\rho_{\pi}$ in $\rho_{\pi}^{a}$. The mixing results agree very well with our data. Our $\sigma - \pi$ mixing model can explain our measurements quite well. The physics behind this model is the following.

In graphite, the basal plane is a symmetry plane. The $2p_z$ orbital is odd under reflection in this plane, while the $2s$, $2p_x$ , and $2p_y$ are even under reflection. Thus, $2p_z$ does not mix with $2s$, $2p_x$ or $2p_y$. In a-C, the long-range symmetry is broken, but the local symmetry is not known. In one extreme, $2p_x$, $2p_y$ and $2p_z$ equally mix with $2s$ orbitals forming a tetrahedral random network. In the opposite limit, there may be large regions of graphitic structure which bend and twist on a large length scale, say thousands of angstroms. The question is, what happens between these two limits? Our model is that the bonding remains $sp^2$, but the twisting and bending is on a shorter length scale resulting in significant $\sigma - \pi$ mixing.

Viewed from the energy aspect, our model also suggests why the energy splitting between the upper and the lower bands is the same in a-C as in graphite. In graphite, three valence electrons form hybridized $sp^2$ orbitals. At the $\Gamma$ -point, the phase of the $sp^2$ orbitals in the upper two $\sigma$ valence bands is such that the bands have P-symmetry[2,107]. At this point, those two bands are degenerate and about 5 eV below the Fermi energy. Also at the $\Gamma$ -point, the phase of the $sp^2$ orbitals is such that the lower band has S-symmetry. The energy level is about 21 eV below the Fermi energy. The valence $\pi$ band is derived from $2p_z$ atomic orbitals, with their nodal plane being the basal plane. At the $\Gamma$ -point, the energy level is about 8 eV below the Fermi energy. In the strained layer model of Egrun[80,85], the bending of layers makes the energy level of the $\pi$ band move closer to the Fermi energy, because the bonding energy of adjacent $\pi$ orbitals decreases as a function of the angle between the axes of the $P_z$ orbitals(bonding is maximum when the angle is zero [64]). Any perturbation that couples two energy levels will push them apart, the splitting depends on the strength of the perturbation. But it is also inversely proportional to the difference between the energy levels. Thus, the mixing of the $\pi$ band with the upper two $\sigma$ bands will compensate for the decrease in bonding energy due to the misalignment of the $P_z$ orbitals. The mixing of the lowest $\sigma$ band with the $\pi$ band also tends to push the $\pi$ band towards the Fermi energy, but the effect of the lowest $\sigma$ band is much smaller than that of the upper two $\sigma$ bands because the energy splitting is larger ( $E_\pi - E_{\sigma_1} = 13eV$, $E_{\sigma_{2,3}} - E_\pi = 3eV$ ). A full calculation is required

to determine whether these qualitative arguments correctly explain the remarkable similarity between the band structure of graphite and a-C.

A detailed analysis of the measured band structure is also limited by our instrumental resolution. As discussed previously, when q approches the Brillouin zone boundary, our resolution can not resolve the peaks. Therefore, it is somewhat uncertain to rely on the data for $q > 1.75\text{Å}^{-1}$ in our data analysis. Fortunately, our $\sigma - \pi$ mixing model is mainly based on small q data because the discrepancy between our data and graphite after the angular average is in the small q region in which data can be resolved by our spectrometer.

# 3. Conclusion

The spectral momentum density of graphite has been measured for momentum in the basal plane and for momentum parallel to the c-axis of the crystal. The results were compared to a first-principles calculation of the spectral density and excellent agreement was found. This is a further confirmation of the power and accuracy of the density functional theory. Viewed from another perspective, graphite has been investigated by several experimental and theoretical techniques and the electronic structure of this material is well understood, certainly at the level of $\sim$ 1 eV accuracy. The agreement between our measurements and the theoretical calculation of the spectral density provides evidence that the assumptions and approximations in the derivation of the (e,2e) cross section are valid. The agreement further demonstrates that (e,2e) spectroscopy gives sensible results when applied to a system which is well characterized. The technique can be extended with confidence now to other materials, such as amorphous solids, where the electronic structure is less well understood.

The spectral momentum density of two forms of ion sputtered a-C also has been measured. One was made using low RF power (200 W), referred to as the low power sample

and the other was made at high RF power (1000 W), referred to as the high power sample. The results are the same for both samples within our resolution and statistics. We observed two well defined bands which were also observed for evaporated a-C[16]. We show from the integral of the spectral density of these bands that there is almost no $sp^3$ bonding in our samples which is definitely different from Savvides's results. Saavides's analysis would suggest that we should see about 45 % $sp^3$ bonding in our samples. Our (e,2e) results are very similar to the spectral densities of graphite except at small q around 8 eV. The spectral momentum densities in this region of phase space are significantly larger than those of graphite. We propose a new hybridization model of $\sigma - \pi$ mixing to explain this discrepancy successfully.

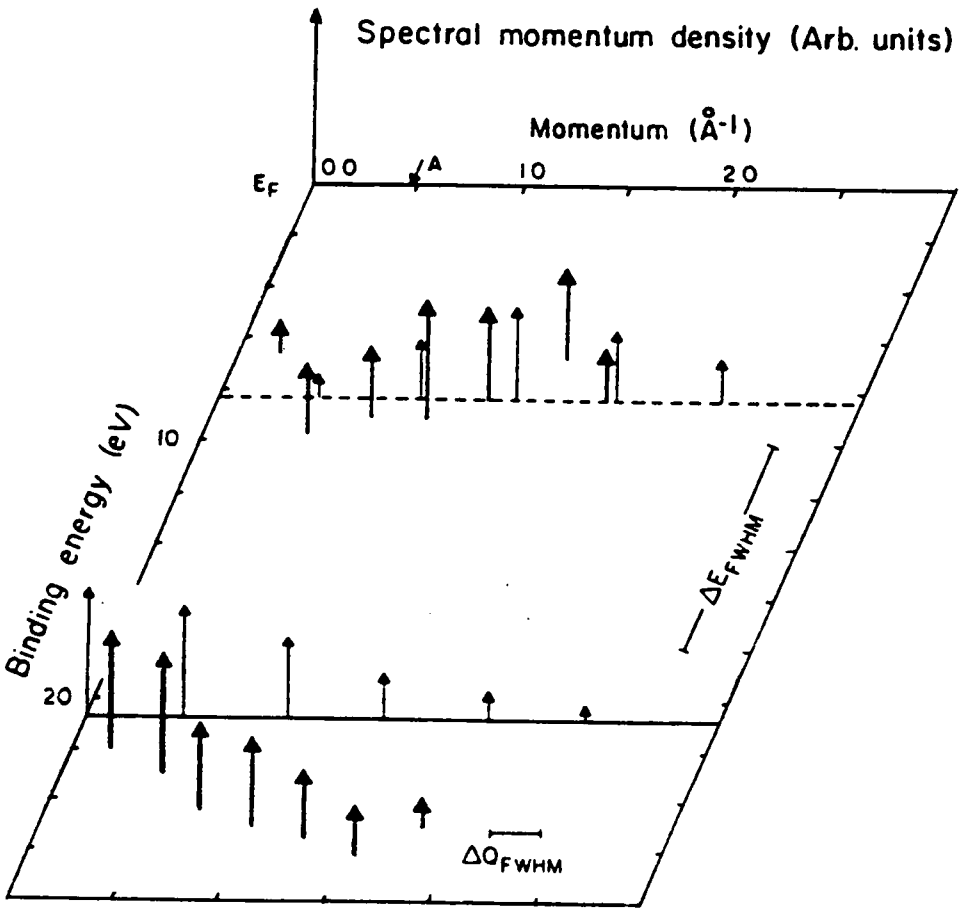


Fig. 10. The spectral densities of graphite as a function of momentum and energy. The momentum is parallel to the c-axis ($\Gamma \rightarrow A$) with a constant component perpendicular to the c-axis $q = -0.35\text{Å}^{-1}$. The dashed and solid lines are the $\pi$ and $\sigma$ bands, respectively. The light arrows are the theoretical spectral densities and the heavy arrows are the measured spectral densities from Table 2.

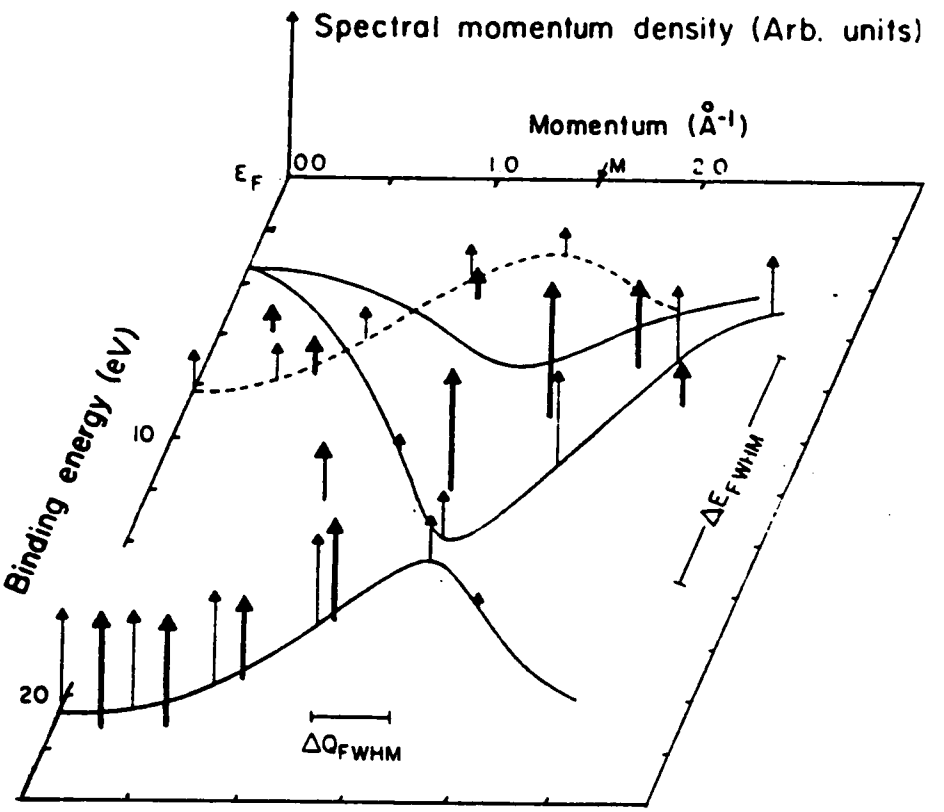


Fig. 11. The spectral densities of graphite as a function of momentum and energy. The momentum is perpendicular to the c-axis (theoretical curves are for $\Gamma \rightarrow M$ direction) with a constant component parallel to the c-axis $q_{Pz} = -0.61\text{Å}^{-1}$. The dashed and solid lines are the $\pi$ and $\sigma$ bands, respectively. The light arrows are the theoretical spectral densities and the heavy arrows are the measured spectral densities from Table 3.

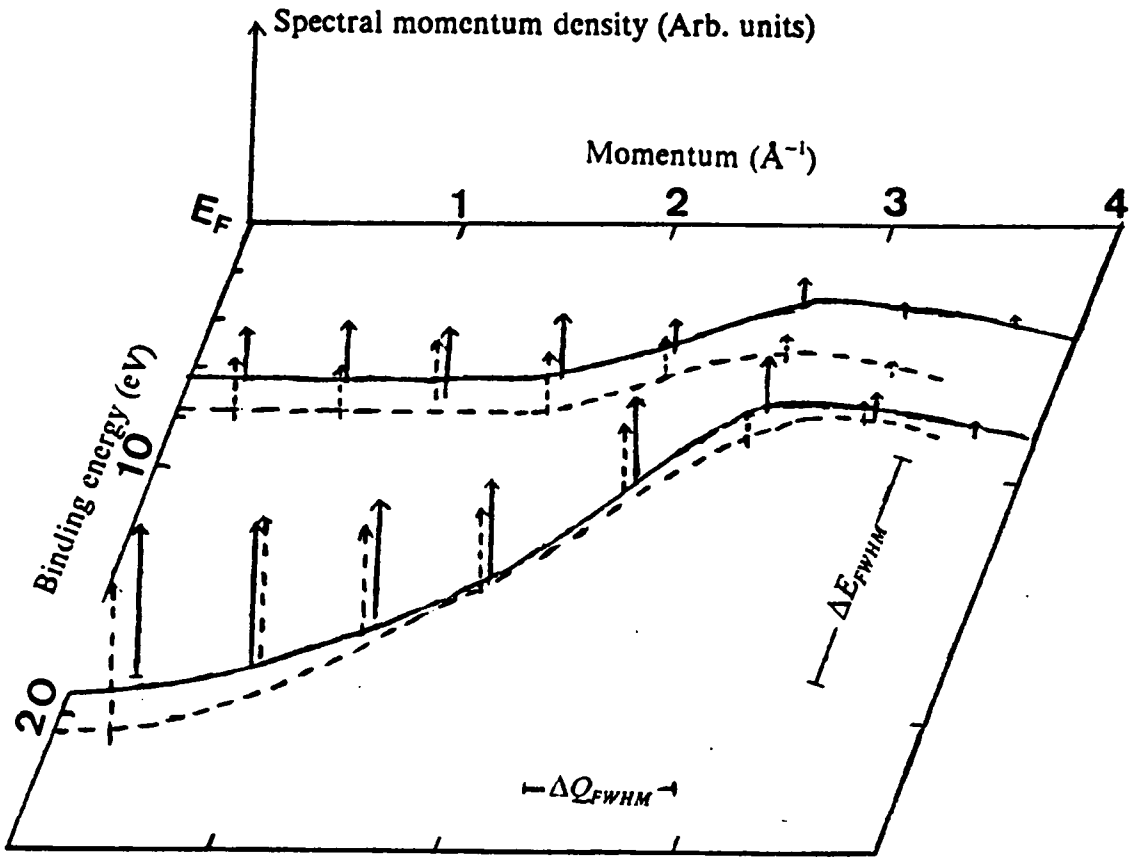


Fig. 12. The experimental spectral densities of ion sputtered a-C as a function of momentum and energy. The momentum is perpendicular to the incoming electron beam with a constant component parallel to the incoming electron beam $q = -0.4\text{Å}^{-1}$. The solid arrows are the measured spectral densities from Table 4 for the high power sample and the dashed arrows are the measured spectral densities from Table 5 for the low power sample.

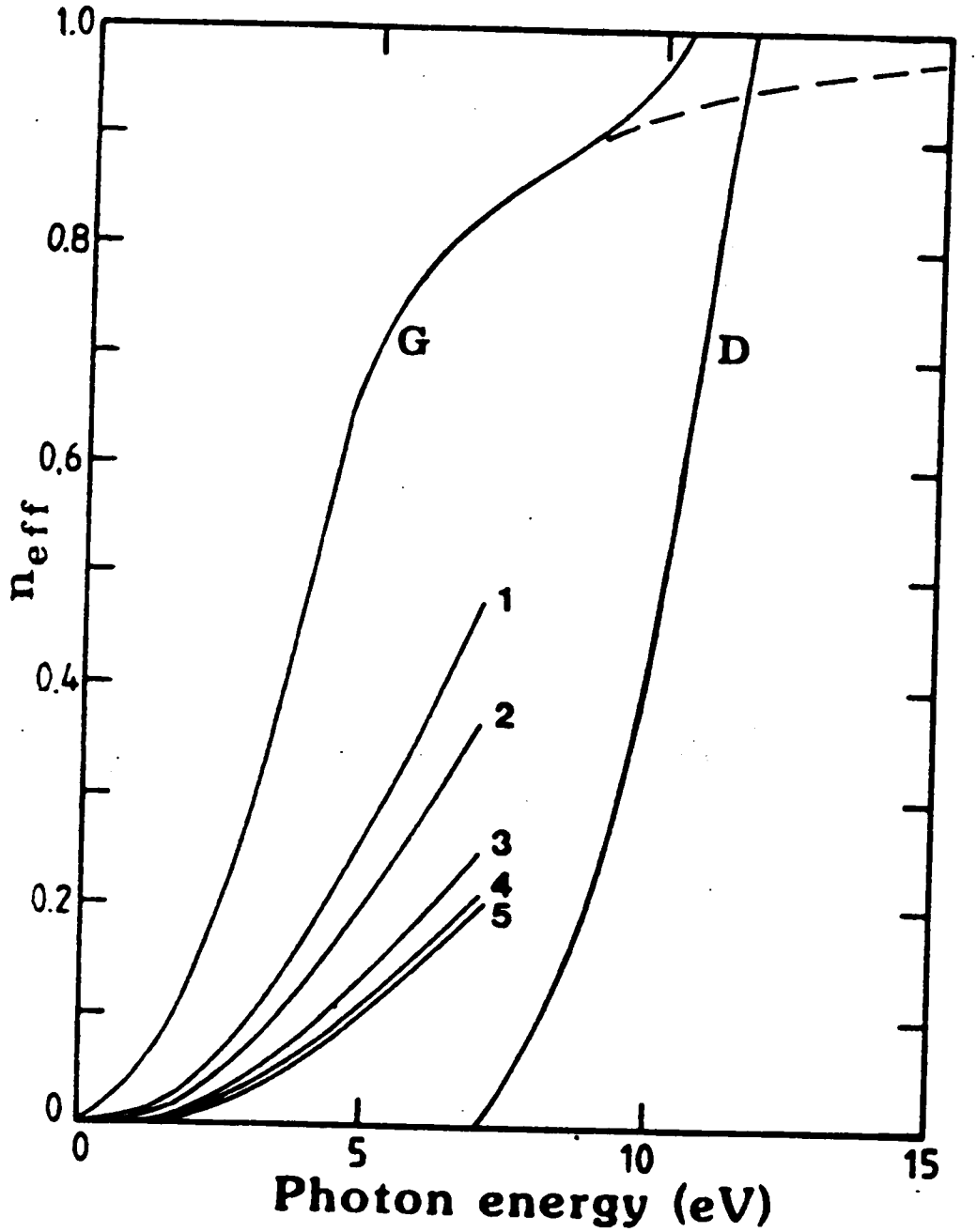


Fig. 13. The effective number of valence electrons $n_{eff}$ per carbon atom taking part in optical transitions vs photon energy. Curves 1-5 represent films made at power 500, 50, 20, 10, and 5W, respectively. Curve G represents graphite(electrical field perpendicular to c axis); the dashed curve shows the $\pi$ component for graphite. Curve D represents diamond[22].

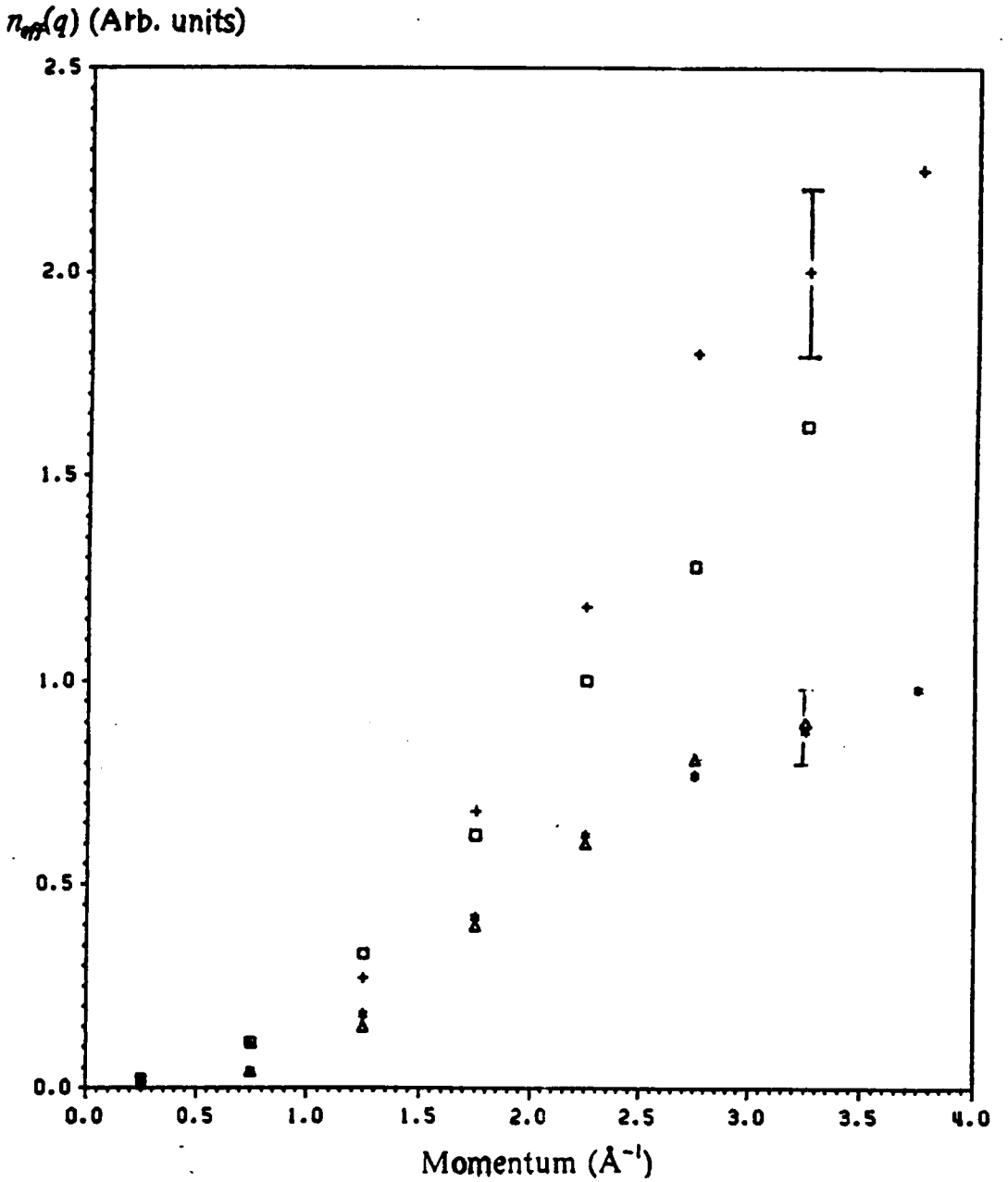


Fig. 14. The number of electrons occupying each band as a function of momentum for ion sputtered a-C. The pluses and the stars are the number of electrons in the bottom and the upper bands for the high power sample, respectively. The squares and the triangles are the number of electrons in the bottom and the upper bands for the low power sample, respectively.

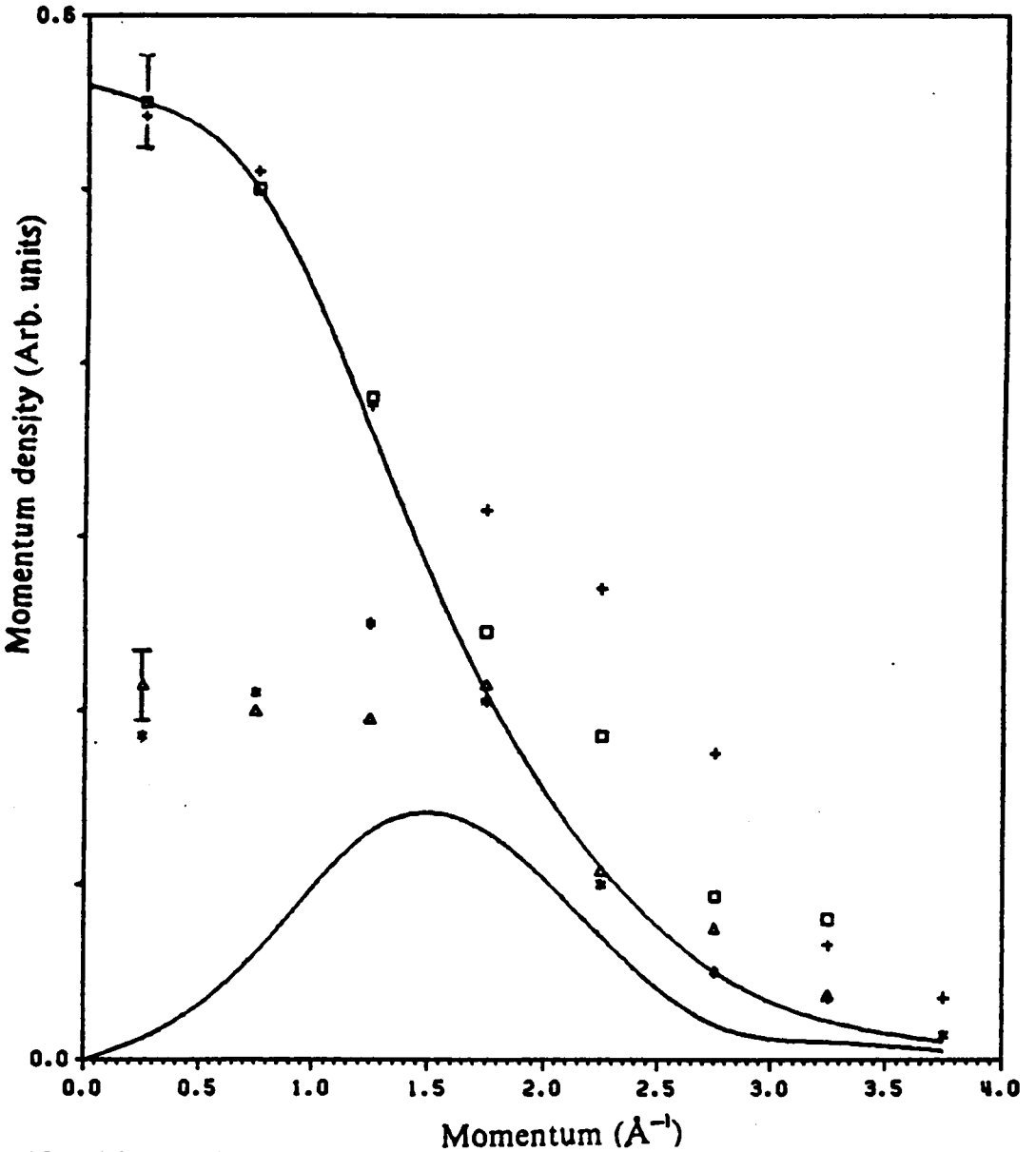


Fig. 15. The experimental momentum densities of ion sputtered a-C as a function of momentum. The momentum is perpendicular to the incoming electron beam with a constant component parallel to the incoming electron beam $q = -0.4\text{Å}^{-1}$ The pluses and the stars are the measured spectral densities of the bottom and the upper bands from Table 4 for the high power sample, respectively; the squares and the triangles are the measured spectral densities of the bottom and the upper bands from Table 5 for the low power sample, respectively. The upper solid curve is the spectral density of the $\sigma$ bands of graphite after a simple angular average; the lower solid curve is the spectral density of the $\pi$ band of graphite after an angular average.

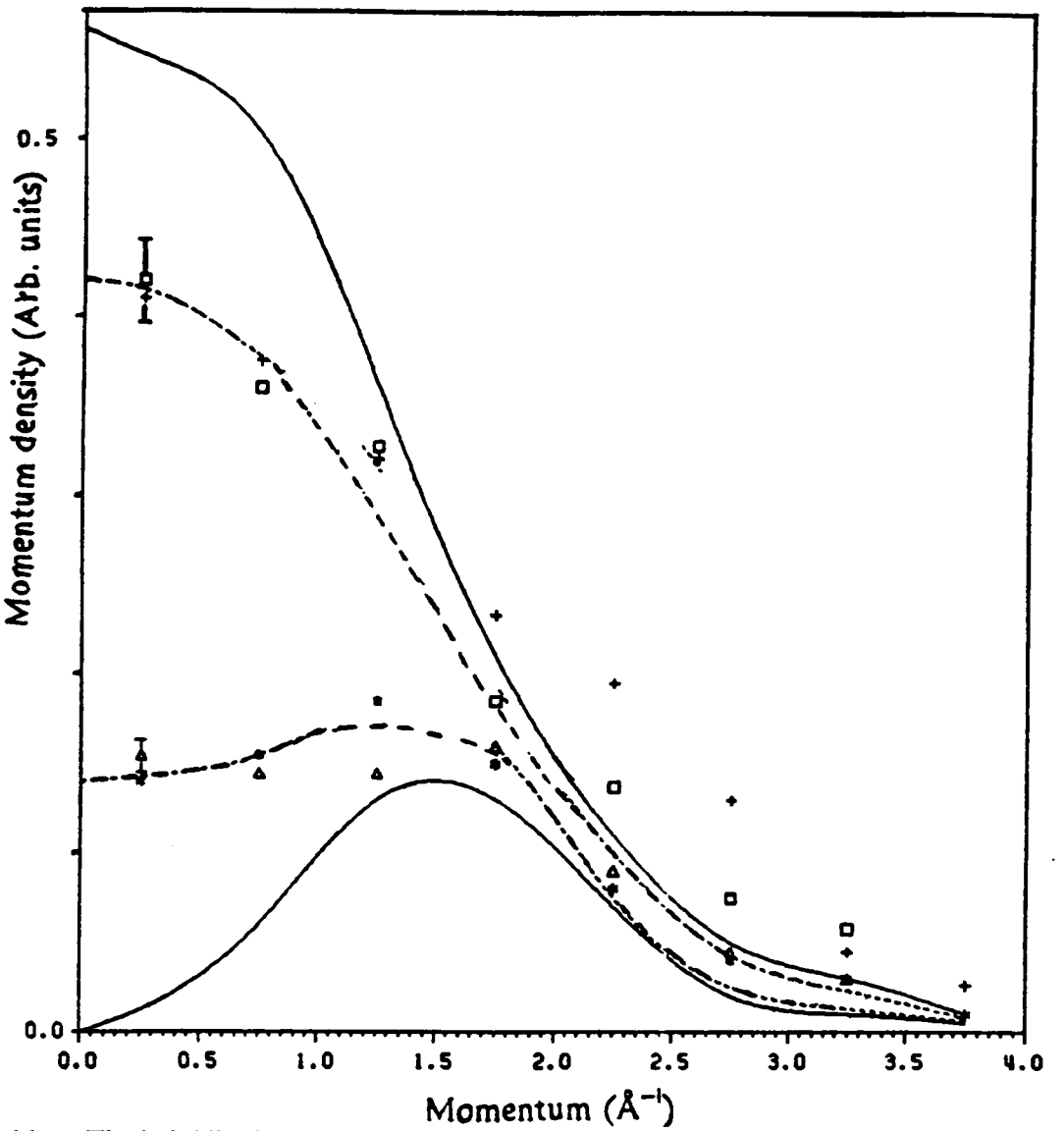


Fig. 16. The hybridized momentum densities of ion sputtered a-C as a function of momentum. The momentum is perpendicular to the incoming electron beam with a constant component parallel to the incoming electron beam $q = -0.4\text{Å}^{-1}$. The pluses and the stars are the measured spectral densities of the bottom and upper bands from Table 4 for the high power sample, respectively; the squares and the triangles are the measured spectral densities of the bottom and the upper bands from Table 5 for the low power sample, respectively. The upper solid curve is the spectral density of the $\sigma$ bands of graphite after a simple angular average; the lower solid curve is the spectral density of the $\pi$ band of graphite after an angular average. The upper and lower dashed curves are the spectral densities after $\sigma - \pi$ mixing with $\alpha = 0.58$ in equations IV.5 and IV.6, respectively.

# Bibliography


1. A. L. Ritter, J. R. Dennison, and J. Dunn, Rev. Sci. Inst. 55, 1280 (1984).

2. J. R. Dennison, Ph.D Thesis, Virginia Polytechnic Institute and State University (1985).

3. N. A. W. Holzwarth, Steven G. Louie, and Shrab Rabii, Phys. Rev. B26, 5382 (1982).

4. A. Bianconi, S. B .M. Hagstrom, and R. Z. Bachrach, Phys. Rev. B16, 5543 (1977).

5. W. Eberhardt, I. T. McGovern, E. W. Plummer, and J. E. Fisher, Phys. Rev. Lett. 44, 200 (1980).

6. A. R. Law, M. T. Johnson, and H. P. Hughes, Phys. Rev. B34, 4289 (1986).

7. F. R. McFeely, S. P. Kowalczyk, L. Ley, R. G. Cavell, R. A. Pollak, and D. A. Shirley, Phys. Rev. B9, 5268 (1974).

8. D. Marchand, C. Fretigny, M. Lagues, F. Batallan, Ch. Simon, I. Rosenman, and R. Pinchaux, Phys. Rev. B30, 4788 (1984).

9. T. Takahshi, H. Tokailin, and T. Sagawa, Solid State Commun. 52, 765 (1984).

10. A. R. Law, J. J. Barry, and H. P. Hughes, Phys. Rev. B28, 5332 (1983).

11. I. T. McGovern, W. Eberhardt, E. W. Plummer, and J. E. Fischer, Physica (b)99, 415 (1980).

12. P. M. Williams, D. Latham, and J. Wood, J. Electron Spectrosc. and Rela. Phenom. 7, 281 (1975).

13. R. F. Willis, B. Feuerbacher, and B. Fitton, Phys. Rev. B4, 2441 (1971).

14. I. E. McCarthy and E. Weigold, to be published in Reports on Progress in Physics.

15. V. G. Levin, V. G. Neudachin, and Yu. F. Smirnov, Phys. Stat. Sol. (b)49, 489 (1972).

16. A. L. Ritter, J. R. Dennison, and R. Jones, Phys. Rev. Lett. 53, 2054 (1984).

17. J. L. Beeby and T. M. Hayes, Phys. Rev. B32, 6464 (1985).

18. R. Haydock, to be published.

19. U. Amaaldi, A. Egidi, R. Marconero, and G. Pizzella, Rev. Sci. Instrum. 40, 1001 (1969).

20. R. Gamilloni, A. Giardini Guidoni, R. Tiribelli, and G. Stefani, Phys. Rev. Lett 29, 618 (1972).

21. B. Lohmann and E. Weigold, Phys. Lett. 86 A, 139 (1981).

22. N. Savvides, J. Appl. Phys. 58(1), 518 (1985).

23. N. Savvides, J. Appl. Phys. 59(12), 4133 (1986).

24. R. H. Ritchie, Phys. Rev. 106, 874 (1957).

25. K. D. Sevier, Low Energy Electron Diffraction (Wiley, New York, 1972)

26. P. Nozieres and D. Pines, Phys. Rev. 113, 1254 (1959).

27. M. T. Yin and M. L. Cohen, Phys. Rev. B29, 6996 (1984).

28. M. T. Yin and M. L. Cohen, Phys. Rev. Lett. 50, 2006 (1983).

29. E. Weigold and I. E. McCarthy, Adv. At. Mol. Phys. 14, 127 (1978).

30. K. T. Leung and C. E. Brion, Journ. of Elect. Spectros. and Rel. Phenom. 35, 327 (1985).

31. G. Stefani, R. Camilloni, and A. Giardini Guidoni, Phys. Lett. (a)64, 364 (1978).

32. H. J. F. Jansen and A. J. Freeman, Phys. Rev. B35, 8207 (1987).

33. R. C. Tatar and S. Rabii, Phys. Rev. B25, 4126 (1982).

34. A. Zunger, Phys. Rev. B17, 626 (1978).

35. A. Bianconi, S. B. M. Hagstrom, and R. Z. Backrach, Phys. Rev. B16, 5543 (1977).

36. H. Nagayoshi, K. Nakao, and Y. Uemora, J. Phys. Soc. Jpn. 41, 1480 (1976).

37. R. F. Willis, B. Fitton, and G. S. Painter, Phys. Rev. B9, 1926 (1974).

38. I. L. Spain, in Chemistry and Physics of Carbon, edited by P. L. Walker and P. A. Thrower (Dekker, New York, 1973), Vol. 8, p.1.

39. G. S. Painter and D. F. Ellis, Phys. Rev. B1, 4747 (1970).

40. J. Dieleman and F. H. M. Sanders, Solid State Technol. 27, 191 (1984).

41. Chao Gao, A. L. Ritter, J. R. Dennison, and N. A. W. Holzwarth, Phys. Rev. B 37, 3914 (1987).

42. N. A. W. Holzwarth, Privite Communication (1988)

43. T. Noda, M. Inagaki, and Y. Yamada, J. Non - Cryst. Solids 1, 285 (1969).

44. M. Nobes, J. Sci. Instrum. 42, 753 (1965).

45. J. J. Hauser, J. Non - Cryst. Solids 23, 21 (1977).

46. S. Aisenberg and R. W. Chabot, J. Appl. Phys. 42, 2953 (1971).

47. S. Aisenberg and R. W. Chabot, J. Vac. Sci. Technol. 10, 104 (1973).

48. C. Weissmantel, K. Bewilogua, D. Dietrich, H. J. Erler, H. J. Hinneberg, S. Klose, W. Noswick, and G. Reisse, Thin Solid Films 72, (1980).

49. L. Holland, U. K. Patent No. 1 582, 231 (August 1976).

50. H. Konig and G. Helwig, Z. Phys. 129, 491 (1951).

51. H. Schmellenmeier, Exp. Tech. Phys. 1, 49 (1953).

52. H. Schmellenmeier, Z. Phys. Chem. 205, 349 (1955-1956).

53. D. S. Whitmell and R. Williamson, Thin Solid Films 35, 255 (1973).

54. L. Holland and S. M. Ojha, Thin Solid Films 38, L17 (1976).

55. L. Holland and S. M. Ojha, Thin Solid Films 58, 107 (1979).

56. D. A. Anderson, Philos. Mag. 35, 17 (1977).

57. C. Weissmantel, K. Bewilogua, H. J. Erler, Hinneberg, S. Klose, W. Nowick, and G. Reisse, Proc. Int. Conf. on Low Energy Ion Beams, In Inst. Phys. Conf. Ser. 54, 188 (1980).

58. A. R. Nyaiesh and W. B. Nowak, J. Vac. Sci. Technol. A1, 308 (1983).

59. E. G. Spencer, P. H. Schmidt, D. J. Joy, and F. J. Sanssalone, Appl. Phys. Lett. 29, 118 (1976).

60. N. N. Matyushenko, V. E. Strelnitskii, and V. A. Gusev, JETP Lett. 30, 199 (1979).

61. G. Gautherin and C. Weissmantel, Thin Solid Films 50, 135 (1978).

62. N. Savvides, J. Appl. Phys. 55, 4232 (1984).

63. C. Weissmantel, K. Bewilogua, K. Breuer, D. Dietrich, U. Ebersbach, H. J. Erler, B. Rau, and G. Reisse, Thin Solids Films 96, 31 (1982).

64. J. Robertson, Advances in Phys. 35, 317 (1986).

65. Michael Frenklach and Karl E. Spear, J. Mater. Res. 3, 133 (1988).

66. J. Zelez, J. Vac. Sci. Technol. A 1(2), 308 (1983).

67. F. J. Kampa and R. W. Grittith, Solar Cell 2, 385 (1980).

68. P. A. Longeway, R. D. Esies, and H. A. Weaklhm, J. Phys. Chem 88, 73 (1984).

69. N. Wada, P. J. Gaczi, and S. A. Solin, J. Non - Cryst. Soliods 35/36, 543 (1980).

70. J. Fink, T. Muller-Heinzerling, and J. Pfluger, Solid State Commun. 47, 687 (1983).

71. J. Fink, T. Muller-Heinzerling, J. Pfluger, and B. Scheerer, Phys. Rev. B 30, 4713 (1984).

72. J. W. Rouzaud and A. Oberlin, Thin Solid Films 105, 75 (1983).

73. D. R. McKenzie, R. C. McPhedran, N. Savvides, and L. C. Botten, Philos. Mag. 48, 341 (1983).

74. Y. Wang and A. L. Ritter, To be published.

75. T. Mori and Y. Namda, J. Vac. Sci. Technol. A 1, 23 (1983).

76. B. Dischler, A. Bubenzer, and P. Koidl, Solid State Commun. 48, 105 (1983).

77. F. N. Smith, J. Appl. Phys. 55, 764 (1984).

78. D. F. R. Mildner and J. M. Carpenter, J. Non -Cryst. Solids 47, 391 (1982).

79. T. Noda, M. Inagaki, and S. Yamada, Bull. Chem. Soc. Jap. 41, 3023 (1968).

80. S. Egrun, Carbon 14, 139 (1976).

81. B. T. Boiko, L. S. Palantik, and A. S. Deveryanchenki, Sov. Phys. Dokl, 13, 237 (1968).

82. J. Kakinoki, K. Katada, T. Hanawa, and T. Ino, Acta Cyystallogr. 13, 171 (1960).

83. D. F. R. Mildner and J. M. Carpenter, Amorphous Semiconductors, Edited by J. Stuke (London, 1974)

84. D. F. R. Mildner and J. M. Carpenter, J. Non - Cryst. Solids 47, 391 (1982)

85. S. Egrun, Acta Crystallogr. a 29, 605 (1973).

86. B. J. Stenhouse and P. J. Grout, J. None - Cryst. Solids 27, 247 (1978).

87. R. E. Franklin, Acta Crystallogr. 3, 107 (1950).

88. G. C. Summerfield, D. F. R. Mildner, and J. M. Carpenter, J. Non - Cryst. Solids 57, 289 (1983).

89. D. Beeman, J. Silverman, R. Lynels, and M. R. Anderson, Phys. Rev. B 30, 870 (1984).

90. D. E. Polk, J. Non - Cryst. Solids 5, 365 (1971).

91. R. Grigorouici, Amorphous and Liquid Semiconductors, Edited by J. Tauc (Plenum, London, 1974).

92. J. M. Zeeman, J. Phys. C4, 3129 (1971).

93. J. M. Zeeman, Models of Disorder (Combridge Univ. Press, London, 1979)

94. R. O. Dillon, John A. Wollam, and V. Katkanant, Phys. Rev. B29, 3482 (1982).

95. P. Lespade, R. Al-Jishi, and M. S. Dresselhaus, Carbon 20, 427 (1982).

96. R. J. Nemanich and S.A. Solin, Phys. Rev. B20, 392 (1979).

97. F. Tuinstra and J. L. Koenig, J. Chem. Phys. 53, 1126 (1970).

98. F. Wooten, Optical Properties of Solids (Acdemic Press, New York and London, 1972).

99. H. Ehrenreich, H. R. Phillip, and B. Segall, Phys. Rev. 132, 1918 (1963).

100. B. R. Cooper, H. Ehrenreich, and H. R. Phillip, Phys. Rev. 138, A494 (1965).

101. R. Jones and A. L. Ritter, J. Electron Spectroscopy and Related Phenomena 40, 285 (1986).

102. P. H. Van Cittert, Z. Phys. 69, 298 (1931).

103. J. Daniels, C. Von Feslenberg, H. Raether and K. Zepperfeld, Springer Tracts in Mod. Phys. 54, 77 (1970).

104. K. Zeppenfeld, Z. Phys. 211, 391 (1968).

105. H. Venghaus, Phys. Status Solidi (b)71, 609 (1975).

106. C. J. Powell, Journal of the Optical Society of America 59, 738 (1969).

107. P. R. Wallace, Phys. Rev. 71, 622 (1947).

108. G. P. Lepage, J. Computational Physics 27, 192 (1978).

109. J. R. Dennison and A. L. Ritter, to be published in Phys. Rev. B.

# Appendix A

In a typical (e,2e) experiment on thin films, the target thickness is comparable to the mean free path for small angle scattering. Jones and Ritter[101] have shown that the (e,2e) coincidence rate, $R$, for a film of thickness $\Delta$ can be written as the convolution of a "smearing function", $S$, with the differential inverse mean free path for (e,2e) scattering, $d\Sigma_{(e,2e)}/dEd\Omega_1 d\Omega_2$, which is the quantity of interest.

$$R(\varepsilon, \vec{q}) = I_0 \bullet \Delta \bullet S \; o \; \frac{d\Sigma_{(e,2e)}}{dEd\Omega_1\Omega_2} \; \Delta E \Delta\Omega_1 \Delta\Omega_2 \qquad [A1]$$

where "$o$" is the convolution operation, $I_0$ is the incident current (electrons/sec.), and $\Delta E$, $\Delta\Omega_1$ and $\Delta\Omega_2$ are the experimental resolutions. The differential cross section is related to the differential inverse mean free path by

$$\frac{d\sigma}{dEd\Omega_1 d\Omega_2} = \frac{1}{\rho} \; \frac{d\Sigma}{dEd\Omega_1 d\Omega_2} \qquad [A2]$$

where $\rho$ is the density of target electrons. The smearing function incorporates all kinematically allowed combinations of small angle, elastic and inelastic scattering events which can contribute to the multiple scattering background in the (e,2e) coincidence data. The smearing function can be written as

$$S(\varepsilon, \vec{q}, E, \Delta) = \sum_{je,ke,le,ji,ki,li=0}^{\infty} C_{je,ke,le,ji,ki,li}(E, \Delta)\ K_{je,ke,le,ji,ki,li}(\varepsilon, \vec{q}) \qquad [A3]$$

where $E$ is the incident energy, C is defined in ref. [34], and $K$ is a function of the probability for small angle scattering with total energy loss $\varepsilon$ and total momentum transfer $\vec{q}$. The integer $je(ke,le)$ is the number of elastic scattering events before the (e,2e) collision (after the (e,2e) collision for the scattered, recoiling electron) and $ji(ki,li)$ is the number of inelastic scattering events before the (e,2e) collision (after the (e,2e) collision for the scattered, recoiling electron). The function $K$ integrated over $\varepsilon$ and $\vec{q}$ is normalized to unity. The sum of all the coefficients $C$ is also one. Thus, the term $C_{je,ke,le,ji,ki,li}(E, \Delta)\ K_{je,ke,le,ji,ki,li}(\varepsilon, \vec{q})$ in the function $S$ is the probability that $je + ke + \leq$ elastic scattering events and $ji + ki + li$ inelastic scattering events will occur in a film of thickness $\Delta$ when the energy of the incident beam is $E$, the total energy loss is $\varepsilon$, and the total momentum transfer is $\vec{q}$. The function $K$ is

$$K_{je,ke,le,ji,ki,li} = P_{je,el} \circ P_{ji,in} \circ P'_{ke,el} \circ P'_{ki,in} \circ P''_{le,el} \circ P''_{li,in} \qquad [A4]$$

where

$$P_{n,el} = \lambda_{el} \frac{d^4\Sigma_{el}}{dEd^3q} \circ P_{n-1,el} \qquad [A5]$$

$P_{0,el}$ = resolution function of the incident beam

$$P_{n,in} = \lambda_{in} \frac{d^4\Sigma_{in}}{dEd^3q} \circ P_{n-1,in} \qquad [A6]$$

$$P_{0,in} = \delta(\vec{q})\ \delta(E) \qquad [A7]$$

where $\frac{d^4\Sigma_{el}}{d^3q d\varepsilon} = (\frac{d^3\Sigma_{el}}{d^3q})\ \delta(E)$ and $\frac{d^4\Sigma_{in}}{d^3q d\varepsilon}$ are the differential inverse mean free paths for elastic and inelastic scattering respectively. The factors $\lambda_{el}$ and $\lambda_{in}$ are the mean free paths for elastic and inelastic scattering. The functions $P'$ and $P''$, referring to the scattered and recoiling electrons, are the same as the function $P$ except that the energy of the electrons are roughly half the energy of the incident electron and the coordinate system for the momentum is different for the incident, scattered, and recoiling electrons. Thus, the smearing function is determined by four functions: $\frac{d^4\Sigma_{el}}{d^3q d\varepsilon} = (\frac{d^3\Sigma_{el}}{d^3q})\ \delta(E)$, $\frac{d^4\Sigma_{in}}{d^3q d\varepsilon}$, $P_{0,el}$ and $P'_{0,el}$ (in our spectrometer the resolution functions for the scattered and recoiling electrons, $P'_{0,el}$ and $P''_{0,el}$ are equal). There are several ways to deconvolute $\frac{d\Sigma_{(e,2e)}}{dE d\Omega_1 \Omega_2}$ from the measured coincidence rate. We have used the iterative technique suggested by Van Cittert [35].

$$\Sigma^{(1)}_{(e,2e)} = \frac{2R}{\Delta \times I_0} - \frac{R \circ S}{\Delta \times I_0} \qquad [A8]$$

$$\Sigma^{(n)}_{(e,2e)} = \Sigma^{(n-1)}_{(e,2e)} + \frac{R}{\Delta \times I_0} - \Sigma^{(n-1)}_{(e,2e)} \circ S \qquad [A9]$$

where $\Sigma_{(e,2e)} = (d\Sigma_{(e,2e)}/dE d\Omega_1 \Omega_2)\ \Delta E \Delta\Omega_1 \Delta\Omega_2$. We discuss next the differential inverse mean free path for elastic scattering and then the differential inverse mean free path for inelastic scattering. With these functions, we have calculated $S$ up to second order multiple scattering. We estimate how the cutoff at second order affects the accuracy of $\Sigma_{(e,2e)}$.

Elastic scattering will occur only if the Bragg condition is satisfied. In our scattering geometry to observe target electron momentum $\vec{q}$ in the plane of the film we vary the angle of the incident beam with respect to the normal of the film (See Fig. 2). For our graphite sample the c-axis is normal to the plane of the film. There will be no Bragg scattering when observing electrons with momentum inside the first Brillouin zone. The incident beam will be elastically scattered when the component of the momentum perpendicular to the c-axis first touches the Brillouin zone boundary ($q_{P_e} \cong 1.5 \text{Å}^{-1}$). The Bragg reflection changes the sign of the angle between the incident electron and the c-axis but does not affect the

magnitude of $q_{P_e}$ which is observed. Since the band dispersion and spectral momentum density are invariant under the transformation $\vec{q} \rightarrow -\vec{q}$ the (e,2e) data is not affected by Bragg scattering of the incident beam. The scattered and recoiling electrons leaving the (e,2e) vertex also can be Bragg reflected before they exit from the sample. There will be no scattering of these two electrons until the component of momentum parallel to the c-axis is $q_{P_a} \cong 2.9\text{Å}^{-1}$. This is nearly six times the momentum of the first Brillouin zone boundary in the direction of the c-axis and lies beyond our last data point at $q = 1.84\text{Å}^{-1}$. Thus, for momentum perpendicular and parallel to the c-axis of graphite our (e,2e) data was unaffected by elastic Bragg scattering.

The smearing function to second order contains contributions only from small angle, inelastic scattering of the incident, scattered and recoiling electrons. Since graphite is anisotropic, the differential inverse mean free path for small angle scattering is a tensor which depends on the initial and final direction of the scattered electron. The tensor is diagonal in a coordinate system in which the momentum is measured relative to the c-axis. The differential inverse mean free path written in terms of the dielectric function is [103]

$$\frac{d^4\Sigma_{in}(\varepsilon,\vec{q})}{d^3q d\varepsilon} \simeq \frac{1}{a_0 E}\ Im\left\{\sum_{i,j} \frac{-\ \delta(\vec{q}\cdot\vec{V}/V - \omega_p/V)}{q_i\,\varepsilon_{ij}\,q_j}\right\}$$

$$= \frac{1}{a_0 E}\ Im\left\{\frac{-\ \delta(\vec{q}\cdot\vec{V}/V - \omega_p/V)}{q^2\cos^2\theta\ \varepsilon_{P_a}(\varepsilon,\vec{q}) + q^2\sin^2\theta\ \varepsilon_{P_e}(\varepsilon,\vec{q})}\right\} \qquad [A10]$$

instead of $\frac{1}{q^2} Im \frac{-1}{\varepsilon}$ for an isotropic dielectric function. Where $\hbar \equiv 1$, $a_0$ is the Bohr radius, $E$ is the incident energy, $\theta$ is the angle between $\vec{q}$ and the c-axis, $\varepsilon_{P_a}$ is the dielectric function for $\vec{q}$ parallel to the c-axis, $\varepsilon_{P_e}$ is the dielectric function for $\vec{q}$ perpendicular to the c-axis, $\omega_p$ is the plasmon energy, and $\vec{V}$ is the incident velocity. Measurements[104] of $d^4\Sigma_{in}/d^3q d\varepsilon$ as function of $|\vec{q}|$ show that it is proportional to $1/q^2$ out to a critical momentum $q_c \simeq 1.25\text{Å}^{-1}$

, then it falls off more rapidly than $1/q^2$ . We have made the approximation that $\varepsilon_{P_a}$ and $\varepsilon_{P_e}$ are independent of $q$ for $q \leq q_c$ and that $d^4\Sigma_{in}/d^3q d\varepsilon$ is zero for $q > q_c$ . For the energy dependence of the parallel and perpendicular dielectric function we fit the experimental data of ref.[105] to the Drude-Sellmeier formula [106]. The perpendicular dielectric function was fit with a plasmon energy of 21 eV and the two harmonic oscillators at 15 eV and 4 eV. The damping constants ($\hbar$ /relaxation time) were 3.0 eV, 7.0 eV, and 2.0 eV for the plasmon and two harmonic oscillators, respectively. The oscillator strengths were 0.15, 0.80, and 0.15 respectively. The parallel dielectric function was fit with a plasmon energy of 15.0 eV and three harmonic oscillators at 15.0 eV, 10.0 eV, and 4.0 eV. The respective damping constants were 1.5 eV, 12.0 eV, 0.75 eV, and 2.0 eV. The respective oscillator strengths were 0.35, 0.50, 0.20, and 0.05. These parameters gave an excellent fit for the positions of the small angle, energy loss peaks. The experimental and fitted peak heights differ by less than 3% for momentum parallel to the c-axis and 12% for momentum perpendicular to the c-axis.

For amorphous carbon, the energy loss function can be fitted by the Drude free electron gas model[2,101].

$$Im\frac{-1}{\varepsilon} = \frac{\omega_P^2 \tau \omega}{(\omega^2 - \omega_P^2)^2 \tau^2 + \omega^2} \qquad [A11]$$

The parameters were determined from high resolution EELS data of Wang and Ritter[74]. For the high power sample $\hbar\omega_P = 22.0$ eV and $\hbar/\tau = 15.2$ eV. For the low power sample $\hbar\omega_P = 23.25$ eV and $\hbar/\tau = 17.25$ eV.

The last parameters which enter the smearing function are the target thickness and the mean free path for inelastic scattering. These parameters always appear as a ratio in the smearing function. This ratio can be determined from the multiple scattering peaks associated with elastic scattering of electrons at 45°. In addition to the elastic peak, there are peaks at lower energy corresponding to electrons which have created plasmons either before or after the $\sim 45°$ elastic vertex. The ratios of the plasmon peaks to the elastic peak

can be calculated in the same way as the smearing function. Assuming that the elastic mean free path for graphite is infinite, the ratio of the first plasmon loss peak to the elastic peak is

$$\frac{I_{one-plasmon}}{I_{elastic-peak}} = \frac{C_{10}}{C_{00}} \int dE\, d\vec{q}\; \lambda_{in}\; \frac{d^4\Sigma_{in}(E_P - E, 0 - \vec{q})}{d^3q dE}\; \frac{F(E, \vec{q})}{\Delta E \Delta q_x \Delta q_y \Delta q_z}$$

$$+ \frac{C_{01}}{C_{00}} \int dE\, d\vec{q}\; \lambda_{in}\; \frac{d^4\Sigma'_{in}(E_P - E, 0 - \vec{q})}{d^3q dE}\; \frac{F(E, \vec{q})}{\Delta E \Delta q_x \Delta q_y \Delta q_z}$$

$$= \frac{\Delta}{\lambda_{in}}\, g(\beta) \int dE\, d\vec{q}\; \lambda_{in}\; \frac{d^4\Sigma_{in}(E_P - E, 0 - \vec{q})}{d^3q dE}\; \frac{F(E, \vec{q})}{\Delta E \Delta q_x \Delta q_y \Delta q_z}$$

$$+ \frac{\sqrt{2}\,\Delta}{\lambda_{in}}\, h(\beta) \int dE\, d\vec{q}\; \lambda_{in}\; \frac{d^4\Sigma'_{in}(E_P - E, 0 - \vec{q})}{d^3q dE}\; \frac{F(E, \vec{q})}{\Delta E \Delta q_x \Delta q_y \Delta q_z} \qquad [A12]$$

$$g(\beta) = 1 - 1/\beta + 1/(e^{\beta} - 1) \qquad [A13]$$

$$h(\beta) = 1 + 1/\beta - e^{\beta}/(e^{\beta} - 1) \qquad [A14]$$

$$\beta = (\sqrt{2} - 1)\,\Delta/\lambda_{in} \qquad [A15]$$

$$C_{j,k}(E, \Delta) = \int_0^{\Delta} \frac{dt}{\Delta}\, e^{-\alpha t - \sqrt{2}\,\alpha(\Delta - t)}\; \frac{[\alpha t]^j}{j!}\; \frac{[\gamma(\Delta - t)]^k}{k!}$$

$$= \frac{2^{k/2} e^{-\alpha\Delta}\,(\alpha\,\Delta)^{j+k}}{(\sqrt{2} - 1)\,\alpha\,\Delta\, j!} \sum_{i=0}^{k} \frac{(j+i)!}{i!(k-i)!} \sum_{l=0}^{j+i} \frac{(-1)^{i+l}}{(j+i-l)!} \left[\frac{1}{(\sqrt{2} - 1)\,\alpha\,\Delta}\right]^l$$

$$- \frac{2^{k/2} e^{-\sqrt{2}\,\alpha\Delta}}{(\sqrt{2} - 1)\,\alpha\,\Delta\, j!} \sum_{i=0}^{k} \frac{(j+i)!}{i!\,(k-i)!}\; \frac{(-1)^j\,(\alpha\,\Delta)^{k-i}}{(\sqrt{2} - 1)^{j+i}} \qquad [A16]$$

where $\alpha = 1/\lambda_{in}$, t is the depth at which $\sim 45°$ elastic scattering occurs. $j$ and $k$ denote the numbers of inelastic scattering event before and after $\sim 45°$ elastic vertex. $d^4\Sigma_{in}/d^3q d\varepsilon$ and $d^4\Sigma'_{in}/d^3q d\varepsilon$ are the differential loss functions before and after the 45° elastic scattering event respectively. The resolution function $F(E, \vec{q}) \equiv f(E)\ f(\vec{q})$ is defined such that

$$f(E=0) = f(\vec{q}=0) = 1 \qquad [A17]$$

$$\int f(E)\, dE = \Delta E \qquad [A18]$$

$$\int f(\vec{q})\, d\vec{q} = \Delta q_x\, \Delta q_y\, \Delta q_z \qquad [A19]$$

Fitting the one parameter, $\Delta/\lambda_{in}$ ,to our data we find $\Delta/\lambda_{in} = 0.5$ for an electron of energy 25KeV. The inelastic mean free path is, $\lambda = 220$Å , from integrating $d^4\Sigma_{in}/d^3q dE$ . This implies that t = 110 Å which is consistent with our estimate of the thickness from the attenuation of light.

In the deconvolution of our graphite data, only first and second order terms in the smearing function were calculated(see appendix b). The first order term is the (e,2e) vertex with no other scattering. The second order term is an (e,2e) vertex with one small-angle, inelastic vertex for either the incident, scattered, or recoiling electron. In the deconvolution procedure, the second order term required numerical integration of a four dimensional integral. A third order term would require numerical evaluation of a six dimensional integral. We have estimated the error in our deconvolution procedure from dropping higher order terms in the smearing function by the following argument. Assume the differential inverse mean free path for (e,2e) scattering is zero for binding energies less than the Fermi energy and constant (say $\Sigma^0$ ) for binding energies greater than the Fermi energy. Then it is straightforward to show that the measured coincidence rate at binding energy, $E_B$ , is $\Sigma^0$ times the integral of the smearing function over energy and momentum with the

upper limit on the energy integral equal to $E_B$ . The first order term in the smearing function peaks near $E_B = 0$ (the Fermi energy); the second order term peaks near the plasmon energy (~ 25 eV); the third order term peaks at twice the plasmon energy; and higher order terms peak at even larger binding energies. Our data extends from $E_B$ = -4.4 eV to $E_B$ = 27.6 eV so that only the first and second order terms in the smearing function influence significantly the measured coincidence rate. We have estimated the error due to cutting off the series at the second order by integrating the first, second and third order term in the smearing function over the range of our data. The third order contribution is ~ 6% of the first and second order contribution.

# Appendix B

As discussed in appendix A, there is no elastic scattering in graphite and it is good enough to keep only the first and second order inelastic scattering contribution in the smearing function. Namely

$$S(\varepsilon, \vec{q}, E, \Delta) = \sum_{j,k,l=0}^{\infty} C_{j,k,l}(E, \Delta)\ P_{j,in} \circ P'_{k,in} \circ P''_{l,in} \circ K_{el}^{(0)}$$

$$\simeq \sum_{j,k,l=0}^{1} C_{j,k,l}(E, \Delta)\ P_{j,in} \circ P'_{k,in} \circ P''_{l,in} \circ K_{el}^{(0)} \qquad [B1]$$

with

$$C_{j,k,l}(E, \Delta) = \int_0^{\Delta} \frac{dt}{\Delta} e^{-\alpha t - \gamma(\Delta - t) - \gamma(\Delta - t)} \frac{[\alpha t]^j}{j!} \frac{[\gamma(\Delta - t)]^k}{k!} \frac{[\gamma(\Delta - t)]^l}{l!}$$

$$= \frac{e^{-2\gamma\Delta}\, \alpha^j\, \gamma^{k+l}}{(\alpha - 2\gamma)\Delta} \frac{\Delta^{j+k+l}}{k!\ l!} \sum_{i=0}^{j} \frac{(k + l + i)!}{i!(j - i)!} \sum_{m=0}^{k+l+i} \frac{(-1)^i}{(k + l + i - m)!} \left[ \frac{1}{(2\gamma - \alpha)\Delta} \right]^m$$

$$- \frac{e^{-\alpha\Delta}}{(\alpha - 2\gamma)\,\Delta} \sum_{i=0}^{j} \frac{\alpha^j \gamma^{k+l} \Delta^{j-l}}{(2\gamma - \alpha)^{k+l+i}} \frac{(k + l + i)!\,(-1)^i}{i!\,(j - i)!\,k!\,l!} \qquad [B2]$$

where $\alpha = 1/\lambda_{in}(E)$ , $\gamma = \sqrt{2}/\lambda_{in}(E/2)$, t is the depth at which (e,2e) scattering occurs and j, k, l denote the numbers of inelastic scattering events.

$$K_{el}^{(0)} \equiv P_{0,el} \, o \, P'_{0,el} \, o \, P''_{0,el} = A \, e^{-A_0\varepsilon^2 - a_1(q_x^2 + q_y^2) - a_2 q_x q_y - a_3 q_z^2} \qquad [B3]$$

We have used Gaussian distributions for the energy and momentum resolutions of our spectrometer and neglected the effect of small broadening on the large momentum along the beam axis[2]. In this expression,

$$A_0 = \frac{1}{2(a_\varepsilon^2 + a'^2_\varepsilon + a''^2_\varepsilon)} \qquad a_1 = \frac{a_x^2 + a'^2_x + a''^2_x}{(a'^2_x + a''^2_x)(2a_x^2 + a'^2_x + a''^2_x)}$$

$$a_2 = \frac{2a_x^2}{(a'^2_x + a''^2_x)(2a_x^2 + a'^2_x + a''^2_x)} \qquad a_3 = \frac{1}{2(a_y^2 + a'^2_y + a''^2_y)}$$

$$A = \frac{1}{\pi^2}\,[A_0\, a_3\, (a_1^2 - a_2^2/4)]^{1/2}$$

where $a_\varepsilon(a'_\varepsilon, a''_\varepsilon)$, $a_x(a'_x, a''_x)$ and $a_y(a'_y, a''_y)$ are the energy and momentum resolutions (FWHM) for the incident beam (outgoing beams) respectively. The values are

| | | | |
|---|---|---|---|
| $a_\varepsilon = 1.6$ | $a'_\varepsilon = 2.0$ | $a''_\varepsilon = 2.7$ | $(eV)$ |
| $a_x = 0.13$ | $a'_x = 0.20$ | $a''_x = 0.20$ | $(\text{Å}^{-1})$ |
| $a_y = 0.13$ | $a'_y = 0.20$ | $a''_y = 0.20$ | $(\text{Å}^{-1})$ |

The experimental coincidence rate usually is measured only as a function of one component of momentum. One approximation must be made in deconvolution [101]:

$$\Sigma_{(e,2e)}^{(n)}(q_x = 0, q_y = 0, q_{z,}\varepsilon) \simeq \frac{R(q_x = 0, q_y = 0, q_{z,}\varepsilon)}{\Delta \times I_0} + \Sigma_{(e,2e)}^{(n-1)}(q_x = 0, q_y = 0, q_{z,}\varepsilon)$$

$$- \; S(-q_{1x}, -q_{1y}, q_z, -q_{z1}, \varepsilon - \varepsilon_1) \, o \, \Sigma_{(e,2e)}^{(n-1)}(q_{1x} = 0, q_{1y} = 0, q_{1z,}\varepsilon_1) \qquad [B4]$$

with

$$\Sigma_{(e,2e)}^{(0)} \equiv \frac{R}{\Delta \times I_0} \qquad [B5]$$

in the cartesian coordinates with $\hat{x}, \hat{y}$ along two outgoing beam directions respectively and with $\hat{z}$ perpendicular to the scattering plane ( see Fig. 17). Denoting

$$S_{j,k,l} \equiv C_{j,k,l}\ P_{j,in} \circ P'_{k,in} \circ P''_{l,in} \circ K_{el}^{(0)}$$

then we can calculate $S \circ \Sigma_{(e,2e)}^{(n-1)}$ term by term as following:

$$S_{000} \circ \Sigma_{(e,2e)}^{(n-1)}(\varepsilon,0,0,q_z) = C_{000} P_{0,el}\ P_{0,in} \circ P'_{0,in} \circ P''_{0,in} \circ K_{el}^{(0)} \circ \Sigma_{(e,2e)}^{(n-1)}$$

$$= C_{000} K_{el}^{(0)}(\varepsilon - \varepsilon_1, \vec{q} - \vec{q}_1) \circ \Sigma_{(e,2e)}^{(n-1)}(\varepsilon_1,0,0,q_{1z})$$

$$= C_{000} \int_{-\infty}^{\infty} d\varepsilon_1 dq_{1x} dq_{1y} dq_{1z}\ A\, e^{-A_0(\varepsilon - \varepsilon_1)^2 - a_1[(q_x - q_{1x})^2 + (q_y - q_{1y})^2]}$$

$$\times\ e^{-a_2(q_x - q_{1x})(q_y - q_{1y}) - a_3(q_z - q_{1z})^2}\ \Sigma_{(e,2e)}^{(n-1)}(\varepsilon_1,0,0,q_{1z})$$

$$= \frac{C_{000}\, A}{[a_1^2 - a_2^2/4]^{1/2}} \int_{-\infty}^{\infty} d\varepsilon_1 dq_{1z}\, e^{-A_0(\varepsilon - \varepsilon_1)^2 - a_3(q_z - q_{1z})^2}\ \Sigma_{(e,2e)}^{(n-1)}(\varepsilon_1, 0,0,q_{1z}) \qquad [B6]$$

and

$$S_{100} \circ \Sigma_{(e,2e)}^{(n-1)}(\varepsilon, 0,0,q_z) = C_{100}\ P_{1,in} \circ P'_{0,in} \circ P''_{0,in} \circ K_{el}^{(0)} \circ \Sigma_{(e,2e)}^{(n-1)}$$

$$= C_{100}\ P_{1,in} \circ K_{el}^{(0)} \circ \Sigma_{(e,2e)}^{(n-1)}$$

$$= C_{100}\ \lambda_{in} \frac{d^4\Sigma_{in}}{d^3q d\varepsilon} \circ K_{el}^{(0)} \circ \Sigma_{(e,2e)}^{(n-1)}$$

$$\simeq C_{100} \int d\varepsilon_1 d\varepsilon_2 d\vec{q}_1 d\vec{q}_2\ \delta[(\vec{q} - \vec{q}_1) \cdot \vec{V}/V - \omega_P/V]$$

$$\times\ \frac{\lambda_{in}}{a_0 E}\ Im\left\{ \frac{-1}{\cos^2\theta\ \varepsilon_{Pa}(\varepsilon - \varepsilon_1) + \sin^2\theta\ \varepsilon_{Pe}(\varepsilon - \varepsilon_1)} \right\}$$

$$\times \frac{1}{|\vec{q}-\vec{q}_1|^2}\; K_{el}^{(0)}(\varepsilon_1-\varepsilon_2,\vec{q}_1-\vec{q}_2)\;\Sigma_{(e,2e)}^{(n-1)}(\varepsilon_2,0,0,q_{2z})$$

$$=\frac{C_{100}\lambda_{in}}{a_0E}\;\frac{A}{[a_1^2-a_2^2/4]^{1/2}}\;Im\int_{-\infty}^{\varepsilon}d\varepsilon_1\int_{-\infty}^{\infty}d\varepsilon_2\int_{q_z-q_c}^{q_z+q_c}dq_{1z}\int_{-\infty}^{\infty}dq_{2z}$$

$$\times\int_{-[q_c^2-(q_{1z}-q_z)^2]^{1/2}/2^{1/2}}^{+[q_c^2-(q_{1z}-q_z)^2]^{1/2}/2^{1/2}}\frac{-\sqrt{2}\,dq_{1x}}{\varepsilon_{Pe}(q_z-q_{q1z})^2+\varepsilon_{Pa}\,\omega_P^2/V^2+\varepsilon_{Pe}(\sqrt{2}\;q_{1x}+\;\omega_P/V)^2}$$

$$\times\; e^{-A_0(\varepsilon_1-\varepsilon_2)^2-a_3(q_{1z}-q_{2z})^2}\;\Sigma_{(e,2e)}^{(n-1)}(\varepsilon_2,0,0,q_{2z})$$

$$=\frac{C_{100}\lambda_{in}}{a_0E}\;\frac{A}{[a_1^2-a_2^2/4]^{1/2}}\;Im\int_{-\infty}^{\varepsilon}d\varepsilon_1\int_{-\infty}^{\infty}d\varepsilon_2\int_{q_z-q_c}^{q_z+q_c}dq_{1z}\int_{-\infty}^{\infty}dq_{2z}$$

$$\times\int_{-q_c}^{+q_c}\frac{-dq'_{1x}}{\varepsilon_{Pe}(q_z-q_{q1z})^2+\varepsilon_{Pa}\,\omega_P^2/V^2+\varepsilon_{Pe}(q'_{1x}+\;\omega_P/V)^2}$$

$$\times\; e^{-A_0(\varepsilon_1-\varepsilon_2)^2-a_3(q_{1z}-q_{2z})^2}\;\Sigma_{(e,2e)}^{(n-1)}(\varepsilon_2,0,0,q_{2z})$$

$$=\frac{C_{100}\,\lambda_{in}}{a_0\,E}\;\frac{A}{[a_1^2-a_2^2/4]^{1/2}}\;Im\int_{-\infty}^{\varepsilon}d\varepsilon_1\int_{-\infty}^{\infty}d\varepsilon_2\int_{q_z-q_c}^{q_z+q_c}dq_{1z}\int_{-\infty}^{\infty}dq_{2z}$$

$$\times\;\frac{-\pi}{\sqrt{\varepsilon_{Pe}(\varepsilon-\varepsilon_1)}\;[\varepsilon_{Pe}\;(q_z-q_{1z})^2+\varepsilon_{Pa}\;\omega_P^2/V^2]^{1/2}}$$

$$\times\; e^{-A_0(\varepsilon_1-\varepsilon_2)^2-a_3(q_{1z}-q_{2z})^2}\;\Sigma_{(e,2e)}^{(n-1)}(\varepsilon_2,0,0,q_{2z}) \qquad [B7]$$

A contour integral was employed in last step and the approximation for the dielectric function (see appendix A) was also used so that the integrand outside a circle of radius $q_c$ is zero.

We have done the integration $dq_{1x}\,dq_{1z}$ over a square area instead of a circular area because there is no residue in the region between the circle and the square contour. We have

$$\sin^2\theta\ \left|(\vec{q}-\vec{q}_1)\right|^2 = \left|(\vec{q}-\vec{q}_1)\times\hat{C}\right|^2$$

$$= \frac{1}{2}(q_x - q_{1x} - q_y + q_{1y})^2 + (q_z - q_{1z})^2 = \frac{1}{2}(-q_{1x} - q_{1y})^2 + (q_z - q_{1z})^2$$

$$= \frac{1}{2}(-q_{1x} + q_{1y})^2 + (q_z - q_{1z})^2 = (\sqrt{2}\ q_{1x} + \omega_P/V)^2 + (q_z - q_{1z})^2$$

$$\cos^2\theta\ \left|(\vec{q}-\vec{q}_1)\right|^2 = \left|(\vec{q}-\vec{q}_1)\cdot\hat{C}\right|^2$$

$$= \frac{1}{2}(q_x - q_{1x} + q_y - q_{1y})^2 = \frac{1}{2}(q_{1x} + q_{1y})^2 = \omega_P^2/V^2$$

Where we have used $(\vec{q}-\vec{q}_1)\cdot\vec{V} = \omega_P$ and $\hat{C}$ is the unit vector along the c-axis of graphite. Similarly we can get

$$S_{010}\ o\ \Sigma^{(n-1)}_{(e,2e)}(\varepsilon, 0,0,q_z) = C_{100}\ P_{0,in}\ o\ P'_{1,in}\ o\ P''_{0,in}\ o\ K^{(0)}_{el}\ o\ \Sigma^{(n-1)}_{(e,2e)}$$

$$= C_{100}\ P'_{1,in}\ o\ K^{(0)}_{el}\ o\ \Sigma^{(n-1)}_{(e,2e)}$$

$$= \frac{C_{010}\,\lambda'_{in}}{a_0\,E}\ \frac{A}{[a_1^2 - a_2^2/4]^{1/2}}\ Im\int_{-\infty}^{\varepsilon} d\varepsilon_1 \int_{-\infty}^{\infty} d\varepsilon_2 \int_{q_z - q_c}^{q_z + q_c} dq_{1z} \int_{-\infty}^{\infty} dq_{2z}$$

$$\times \int_{-\infty}^{\infty} \frac{-\,dq_{1y}}{\frac{\varepsilon_{Pe} + \varepsilon_{Pa}}{2}\left[q_{1y} + \frac{\omega_P}{V'}\ \frac{\varepsilon_{Pe} - \varepsilon_{Pa}}{\varepsilon_{Pe} + \varepsilon_{Pa}}\right]^2 + \frac{2\omega_P^2}{V'^2}\ \frac{\varepsilon_{Pe}\,\varepsilon_{Pa}}{\varepsilon_{Pe} + \varepsilon_{Pa}} + \varepsilon_{Pe}\ (q_z - q_{1z})^2}$$

$$\times\ e^{-A_0(\varepsilon_1 - \varepsilon_2)^2 - a_3(q_{1z} - q_{2z})^2}\ \Sigma^{(n-1)}_{(e,2e)}(\varepsilon_2, 0,0,q_{2z})$$

$$= \frac{C_{010}\lambda'_{in}}{a_0 E}\ \frac{A}{[a_1^2 - a_2^2/4]^{1/2}}\ Im\int_{-\infty}^{\varepsilon} d\varepsilon_1 \int_{-\infty}^{\infty} d\varepsilon_2 \int_{q_z - q_c}^{q_z + q_c} dq_{1z} \int_{-\infty}^{\infty} dq_{2z}$$

$$\times \frac{-\sqrt{2}\,\pi}{\sqrt{\varepsilon_{Pe}(\varepsilon-\varepsilon_1)+\varepsilon_{Pa}(\varepsilon-\varepsilon_1)}\left[\varepsilon_{Pe}\,(q_z-q_{1z})^2+\dfrac{2\omega_P^2\,\varepsilon_{Pe}\,\varepsilon_{Pa}}{V'^2\,(\varepsilon_{Pe}+\varepsilon_{Pa})}\right]^{1/2}}$$

$$\times\, e^{-A_0(\varepsilon_1-\varepsilon_2)^2-a_3(q_{1z}-q_{2z})^2}\,\Sigma^{(n-1)}_{(e,2e)}(\varepsilon_2,0,0,q_{2z}) \qquad [B8]$$

Note that

$$S_{001}\,o\,\Sigma^{(n-1)}_{(e,2e)}(\varepsilon,0,0,q_z)=S_{010}\,o\,\Sigma^{(n-1)}_{(e,2e)}(\varepsilon,0,0,q_z) \qquad [B9]$$

because our (e, 2e ) spectrometer has a symmetric coplanar scattering geometry.

In the same way we can get $So\Sigma^{(n-1)}_{(e,2e)}$ for parallel momentum transfer (sweeping $q_x$ instead of $q_z$) except that the coordinate has been rotated around the z axis by 45°(see Fig. 17).

$$S_{000}\,o\,\Sigma^{(n-1)}_{(e,2e)}(\varepsilon,q_x,0,0)=C_{000}\;K^{(0)}_{el}\,o\,\Sigma^{(n-1)}_{(e,2e)}$$

$$=\frac{C_{000}\,A}{[a_3(a_1-a_2/2)]^{1/2}}\int d\varepsilon_1 dq_{1x}$$

$$\times\, e^{-A_0(\varepsilon-\varepsilon_1)^2-(a_1+a_2/2)(q-q_{1x})^2}\,\Sigma^{(n-1)}_{(e,2e)}(\varepsilon_1,q_{1x},0,0) \qquad [B10]$$

$$S_{100}\,o\,\Sigma^{(n-1)}_{(e,2e)}(\varepsilon,q_x,0,0)=C_{100}\;P_{1,in}\,o\,K^{(0)}_{el}\,o\,\Sigma^{(n-1)}_{(e,2e)}$$

$$=\frac{C_{100}\,\lambda_{in}}{a_0E}\cdot\frac{A}{[a_3(a_1-a_2/2)]^{1/2}}\;Im\int_{-\infty}^{\varepsilon}d\varepsilon_1\int_{-\infty}^{\infty}d\varepsilon_2\int_{0-q_c}^{0+q_c}dq_{1z}\int_{-\infty}^{\infty}dq_{2x}$$

$$\times\frac{-\pi}{\sqrt{\varepsilon_{Pe}(\varepsilon-\varepsilon_1)}\,[\varepsilon_{Pe}\,(0-q_{1z})^2+\varepsilon_{Pa}\,\omega_P^2/V^2]^{1/2}}$$

$$\times\, e^{-A_0(\varepsilon_1-\varepsilon_2)^2-(a_1+a_2/2)(q_x-\omega_P/V-q_{2x})^2}\,\Sigma^{(n-1)}_{(e,2e)}(\varepsilon_2,q_{2x},0,0) \qquad [B11]$$

$$S_{010}\, o\, \Sigma^{(n-1)}_{(e,2e)}(\varepsilon, q_x,0,0) = C_{010}\; P'_{1,in}\, o\, K^{(0)}_{el}\, o\, \Sigma^{(n-1)}_{(e,2e)}$$

$$= \frac{C_{010}\,\lambda'_{in}}{a_0 E}\;\; \frac{A}{[a_3(a_1 - a_2/2)]^{1/2}}\;\; Im\int_{-\infty}^{\varepsilon} d\varepsilon_1 \int_{-\infty}^{\infty} d\varepsilon_2 \int_{0-q_c}^{0+q_c} dq_{1y} \int_{-\infty}^{\infty} dq_{2x}$$

$$\times\; \frac{-\sqrt{2}\;\pi}{\sqrt{\varepsilon_{Pe}\;(\varepsilon - \varepsilon_1)}\;[\varepsilon_{Pe}\;(0 - q_{1y})^2 + \varepsilon_{Pa}\;(\sqrt{2}\;\omega_P/V' + q_{1y})^2]^{1/2}}$$

$$\times\; e^{-A_0(\varepsilon_1 - \varepsilon_2)^2 - (a_1 + a_2/2)\,(q_x - q_{2x} + q_{1y} - \sqrt{2}\;\omega_P/V')^2}\;\; \Sigma^{(n-1)}_{(e,2e)}(\varepsilon_2, q_{2x},0,0) \qquad [B12]$$

Again,

$$S_{001}\, o\, \Sigma^{(n-1)}_{(e,2e)}(\varepsilon, q_x,0,0) = S_{010}\, o\, \Sigma^{(n-1)}_{(e,2e)}(\varepsilon, q_x,0,0) \qquad [B13]$$

It is worth paying attention to the position of the residues in applying contour integrals. For example, we need to assure that the contour path encloses one and only one of two residues in order to get equation B8. The residues are

$$q^{+}_{1y} = +i\,f - f_1 = -Im\{f\} - Re\{f_1\} + i(Re\{f\} - Im\{f_1\}) \qquad [B14]$$

$$q^{-}_{1y} = -i\,f - f_1 = +Im\{f\} - Re\{f_1\} - i(Re\{f\} + Im\{f_1\}) \qquad [B15]$$

where

$$f(\varepsilon) = \left[\frac{2\,\varepsilon_{Pe}}{\varepsilon_{Pe} + \varepsilon_{Pa}}\;(q_z - q_{1z})^2 + \frac{\omega_P^2}{V'^2}\;\;\frac{4\,\varepsilon_{Pe}\;\varepsilon_{Pa}}{(\varepsilon_{Pe} + \varepsilon_{Pa})^2}\right]^{1/2}$$

$$f_1(\varepsilon) = \frac{\omega_P}{V'}\;\;\frac{\varepsilon_{Pe} - \varepsilon_{Pa}}{\varepsilon_{Pe} + \varepsilon_{Pa}}$$

In the limit $\omega_P/V' \to 0$ ( $q_z - q_{1z} \neq 0$ then ) or the amorphous case ( $\varepsilon_{Pe} = \varepsilon_{Pa}$ ), it is clear that the contour path encloses one and only one residue because $f_1 = 0$ and $Re\{f\} \neq 0$ due to non zero of imaginary part of the dielectric functions. Since $f$ and $f_1$ are functions of

dielectirc functions which depend on the energy loss, there is possibility that the contour path encloses both residues or none when $(q_z - q_{1z}) \to 0$ . Both cases would make the contour integral zero. It is clear from equation B14 and B15 that we would not run into this trouble as long as

$$|Re\{f\}| > |Im\{f_1\}| \qquad [B16]$$

which assures the two residues not on same side of real axis ( also our integral path ). In the case of $q_z - q_{1z} = 0$, this is the same as

$$|Re\{2\sqrt{\varepsilon_{Pe}\,\varepsilon_{Pa}}\}| > |Im\{\varepsilon_{Pe} - \varepsilon_{Pa}\}| \qquad [B17]$$

Using our fitted dielectric functions equation B14 holds; and also the modules of all residues are less than $q_c \simeq 1.25 \text{Å}^{-1}$. Therefore, we can always enclose one and only one residue in all the contour path integrals we have employed.

As we can see the computation involves four dimensional integrals in both momentum direction investigations. The subroutine VAGAS for multiple dimensional integrals is applied [108]. VAGAS estimates the integrals ($V^n$ = integral volume)

$$I = \int_{V^n} d^n x\, f(\vec{x}) \qquad [B18]$$

by computing the integrand at $N$ random points $\{\vec{x}_i\}_1^n$ in $V^n$ and forming the weighted average:

$$I \simeq S = \frac{1}{N} \sum_{i=1}^{N} \frac{f(\vec{x}_i)}{P(\vec{x}_j)} \qquad [B19]$$

The random points are chosen in $V^n$ with density $P(\vec{x})$ ( $\int_{V^n} d^n x P(\vec{x}) = 1$ ). The approximate uncertainty in $S$ is

$$\sigma^2 = \frac{1}{N-1}\ \frac{1}{N}\ \sum_{i=1}^{N} \frac{f^2(\vec{x}_i)}{P(\vec{x}_i)} \qquad [B20]$$

Theoretically, $\sigma^2$ is minimized when

$$P(\vec{x}) = \frac{|f(\vec{x})|}{\int_{V^n} d^n |f(\vec{x})|} \qquad [B21]$$

That is when sample points $\{\vec{x}_i\}$ are concentrated where the integrand is largest in magnitude.

VEGAS makes m estimates of the integral $\{S_\alpha\}_{\alpha=1}^{m}$. If $N$ is made sufficently large and if $f(\vec{x})$ is square integrable, the central limit theorem implies that the distribution of $S_\alpha$ about $I$ becomes Gaussian. Then $\bar{S}$ is a reliable estimate of $I$, i.e.

$|I - \bar{S}| \leq \bar{\sigma}$ (one standard derivation) with 68% confidence

$\leq 2\bar{\sigma}$ with 95% confidence and so on.

When $f(\vec{x})$ is integrable, but not square integrable, $\bar{S}$ may still converge to $I$. However the error estimates are completely unreliable, in general being too small.

One thing should be noted in using VEGAS, that VEGAS uses first iteration information to locate peaks in $f(\vec{x})$ and then distributes a large portion of the $N$ points in the peak regions. If there are ridges in $f(\vec{x})$ instead of peaks then VEGAS has divergence problem. However, we can get away by using a first iteration ($P(\vec{x}) =$ constant ) and a larger $N$. This is just the simplest form of the Monte Carlo integration method. VEGAS provides not only the integral

result $\overline{S}$ but also the standard derivation $\overline{\sigma}$ which enables users to monitor the accuracy and divergency of the computation.

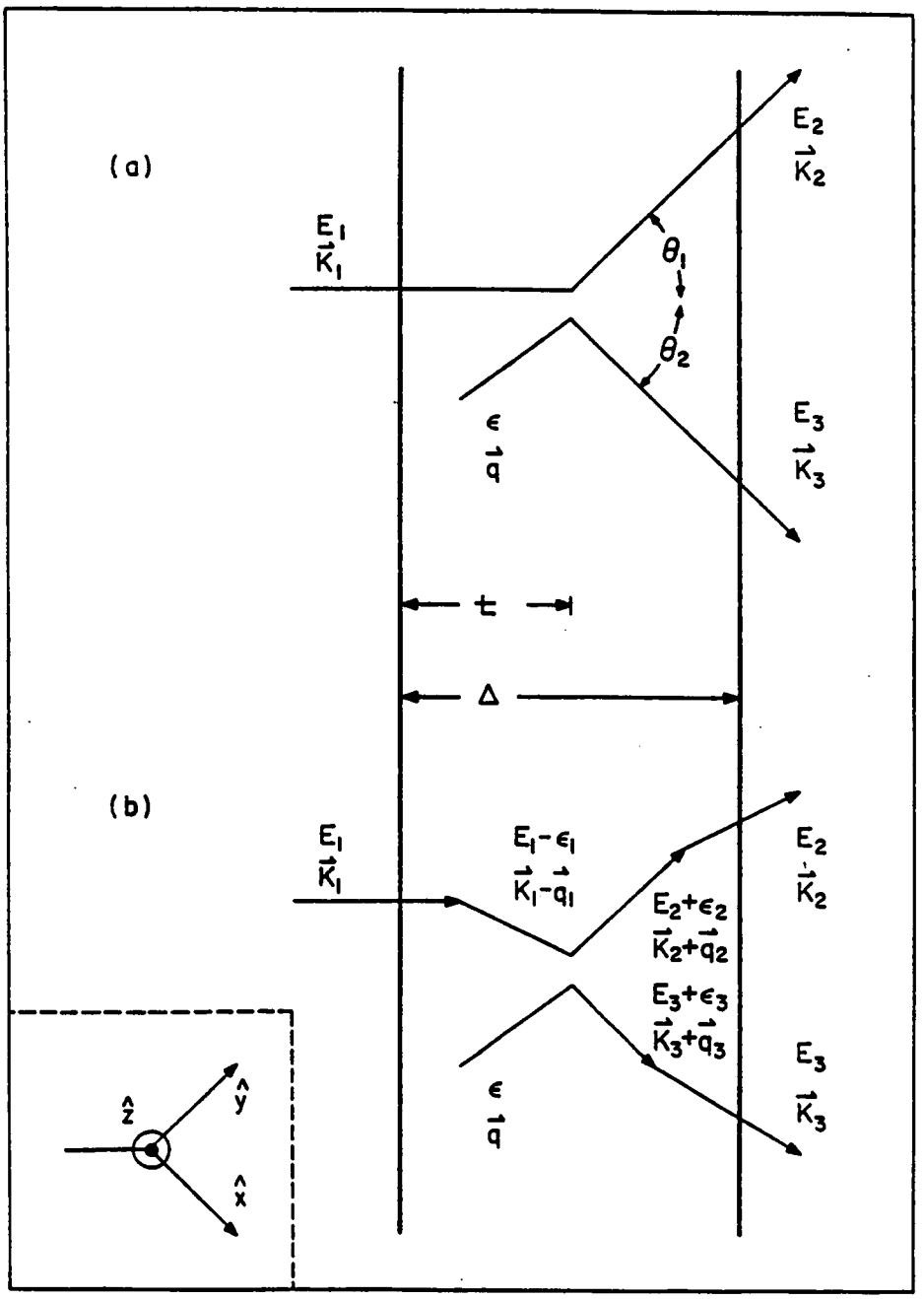


Fig. 17. Kinematics for multiple scattering. (a) An (e,2e) event with no multiple scattering. (b) An (e,2e) event with multiple scattering. The inset is the coordinate system for analysis of the smearing function[101].

**The vita has been removed from the scanned document**